Article

Cell

A Quantitative Multivariate Model of Human Dendritic Cell-T Helper Cell Communication

Graphical Abstract

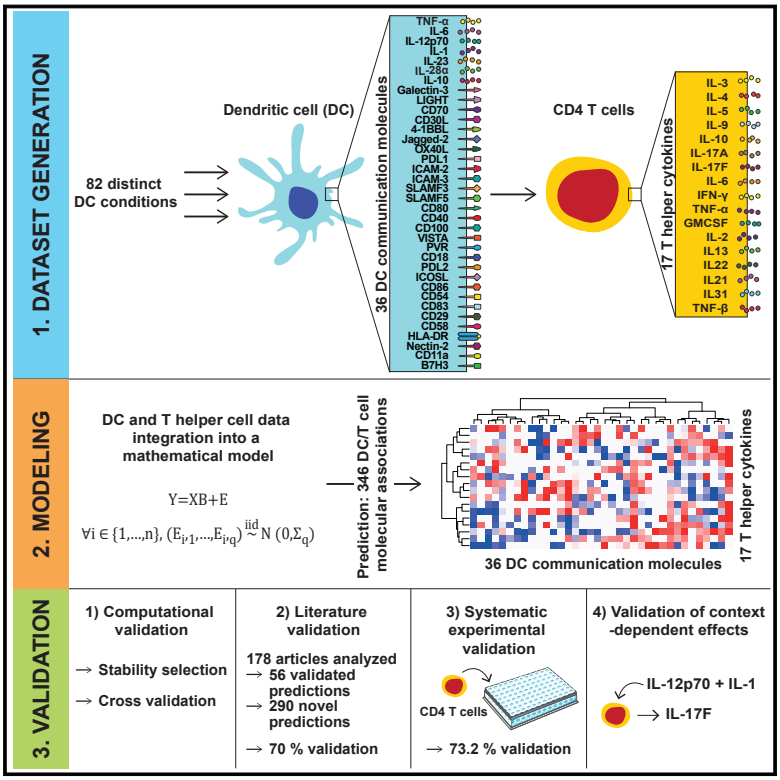

Highlights

- 428 protein-level measurements of 36 DC communication molecules and 17 Th cytokines
- Data-driven quantitative model of DC-T cell communication extensively validated
- Systematic and unbiased predictions of context-dependent mechanisms
- Validation of a new context-dependent role of IL-12p70 in Th17 differentiation

Authors

Maximilien Grandclaudon, Marie Perrot-Dockès, Coline Trichot, ..., Julien Chiquet, Céline Lévy-Leduc, Vassili Soumelis

Correspondence

vassili.soumelis@curie.fr

In Brief

Grandclaudon et al. show that combinatorial rules that explain communication between dendritic cells and T helper cells can be helpful in vaccine design and immunotherapy.

Grandclaudon et al., 2019, Cell *179*, 432–447
October 3, 2019
https://doi.org/10.1016/j.cell.2019.09.012

CellPress

Cell

Article

A Quantitative Multivariate Model of Human Dendritic Cell-T Helper Cell Communication

Maximilien Grandclaudon,[1,2,8] Marie Perrot-Dockès,[3,8] Coline Trichot,[1,2,8] Léa Karpf,[1,2] Omar Abouzid,[1,2] Camille Chauvin,[1,2] Philémon Sirven,[1,2] Wassim Abou-Jaoudé,[4] Frédérique Berger,[1,5,6] Philippe Hupé,[1,6,7] Denis Thieffry,[4] Laure Sansonnet,[3] Julien Chiquet,[3] Céline Lévy-Leduc,[3] and Vassili Soumelis[1,2,9,*]

[1]Institut Curie, Centre de Recherche, PSL Research University, 75005 Paris, France
[2]INSERM U932, Immunity and Cancer, 75005 Paris, France
[3]UMR MIA-Paris, AgroParisTech, INRA—Université Paris-Saclay, 75005 Paris, France
[4]Computational Systems Biology Team, Institut de Biologie de l'École Normale Supérieure, Centre National de la Recherche Scientifique UMR8197, INSERM U1024, École Normale Supérieure, PSL Université, 75005 Paris, France
[5]Institut Curie, PSL Research University, Unit of Biostatistics, 75005 Paris, France
[6]Institut Curie, PSL Research University, INSERM U900, 75005 Paris, France
[7]Mines Paris Tech, 77305 Cedex Fontainebleau, France
[8]These authors contributed equally
[9]Lead Contact
*Correspondence: vassili.soumelis@curie.fr
https://doi.org/10.1016/j.cell.2019.09.012

SUMMARY

Cell-cell communication involves a large number of molecular signals that function as words of a complex language whose grammar remains mostly unknown. Here, we describe an integrative approach involving (1) protein-level measurement of multiple communication signals coupled to output responses in receiving cells and (2) mathematical modeling to uncover input-output relationships and interactions between signals. Using human dendritic cell (DC)-T helper (Th) cell communication as a model, we measured 36 DC-derived signals and 17 Th cytokines broadly covering Th diversity in 428 observations. We developed a data-driven, computationally validated model capturing 56 already described and 290 potentially novel mechanisms of Th cell specification. By predicting context-dependent behaviors, we demonstrate a new function for IL-12p70 as an inducer of Th17 in an IL-1 signaling context. This work provides a unique resource to decipher the complex combinatorial rules governing DC-Th cell communication and guide their manipulation for vaccine design and immunotherapies.

INTRODUCTION

Cell-cell communication involves the exchange of molecular signals produced by a given cell and transmitting an effect through specific receptors expressed on target cells. This process requires integration of multiple communication signals of different nature during homeostatic or stress-related responses. For example, differentiation of pluripotent hematopoietic stem cells into mature myeloid or lymphoid blood cells requires the collective action of multiple cytokines, growth factors, and Notch ligands (Balan et al., 2018). In the context of stress, multiple signals need to be integrated by innate and adaptive immune cells, including cytokines, growth factors, inflammatory mediators, and immune checkpoints (Chen and Flies, 2013; Macagno et al., 2007). In most studies, these communication molecules have been studied as individual stimuli to a target cell by gain- and loss-of-function experiments. This provides important knowledge regarding the downstream effects of the signals but prevents us from widely addressing their function in various contexts of other co-expressed communication signals.

Context dependency is an important aspect of verbal language communication that can directly affect the meaning of individual words but also modify the logic of syntactic rules (Cariani and Rips, 2017; Kintsch and Mangalath, 2011). Similarly, context dependencies may dramatically affect the function of biologically active communication signals. For example, we have shown that 90% of the transcriptional response to type I interferon in human CD4 T cells depends on the cytokine context (T helper 1 [Th1], Th2, or Th17; Touzot et al., 2014). Other studies have identified major context-dependent functions of immune checkpoints, such as OX40-ligand (Ito et al., 2005), and regulatory cytokines, such as transforming growth factor β (TGF-β) (Ivanov et al., 2006; Manel et al., 2008; Volpe et al., 2008). These studies suggest that communication molecules function as words of a complex language with grammar defining combinatorial rules of co-expression and mutual influence of one signal over the function (meaning) of another signal.

Three levels of biological complexity need to be integrated to decipher those combinatorial rules: (1) the multiplicity of input communication signals to include as many possible contextual effects; (2) communication signals at their naturally occurring concentrations; and (3) a large number of output responses in target cells, reflecting the effect of cell-cell communication quantitatively and qualitatively. Those three levels create a bottleneck in deciphering cell-cell communication.

Here we developed an integrative approach combining (1) coupled protein-level measurement of multiple communication signals and output response molecules in target cells; (2) a multivariate mathematical modeling strategy enabling us to infer the input-output relationships for individual signals, taking into account the context and configuration of all other signals; and (3) experimental validation of model-derived hypotheses. We applied this framework to decipher human dendritic cell (DC)-Th cell communication, which potentially involves over 70 individual molecular stimuli (Chen and Flies, 2013), including cytokines, tumor necrosis factor (TNF) family members, integrins, nectins, Notch ligands, and galectins (Tindemans et al., 2017; Zhu et al., 2010; Zygmunt and Veldhoen, 2011). These molecules can all be expressed by DCs and function as communication signals to T cells (hereafter called Th stimuli). They can be measured at the protein level by highly specific assays to optimize biological relevance.

By using this unbiased data-driven approach, we could capture the simultaneous effects of large numbers of DC-T cell communication signals in naturally occurring patterns and expression levels. Our systems-level model revealed novel emergent and context-dependent mechanisms controlling Th cell differentiation. A similar framework can be applied to systematically decipher the communication of other cell types.

RESULTS

Generation of a Unique Multivariate Dataset of Human DC-Th Cell Communication

To induce a broad range of DC molecular states expressing various patterns of communication signals, human monocyte-derived DCs (MoDCs) and primary blood CD11c$^+$ DCs (bDCs), were activated for 24 h with a diversity of DC-modulating signals (hereafter called DC perturbators). These included 14 distinct stimuli that were grouped in three categories reflecting various physiopathological contexts: (1) the endogenous factors interferon β (IFN-β), GM-CSF, TSLP, and PGE2; (2) the Toll-like receptor ligands lipopolysaccharide (LPS) (a Toll-like receptor 4 [TLR4] agonist), PAM3CSK4 (a TLR1 and 2 agonist), Curdlan (a Dectin1 agonist), zymosan (a TLR2 and Dectin1 agonist), R848 (a TLR7 and 8 agonist), poly(I:C) (a TLR3 agonist), and aluminum potassium sulfate (Alum, an NLRP3 inflammasome inducer); and (3) the whole pathogens heat-killed *Candida albicans* (HKCA), heat-killed *Listeria monocytogenes* (HKLM), heat-killed *Staphylococcus aureus* (HKSA), heat-killed *Streptococcus pneumoniae* (HKSP), and influenza virus (flu). These 14 DC perturbators were used in distinct doses and combinations to further increase the diversity of DC communication molecules and downstream functional effects (Table S1). In each independent experiment, we included a medium condition as a negative control and LPS (100 ng/mL) and/or zymosan (10 μg/mL) as positive controls. A total of 66 perturbators were used on MoDCs and 16 on bDCs, totaling 82 distinct "DC conditions" (C1–C82; Table S1).

Under each DC condition, we measured 36 DC-expressed molecules that influence Th cell differentiation in at least one published study (STAR Methods) and can be measured with a highly specific antibody-based assay. Twenty-nine were measured by fluorescence-activated cell sorting (FACS) at the DC surface (Figure S1A), and 7 were measured in the 24-h DC culture supernatant (STAR Methods).

Following 24-h culture under each of the 82 DC perturbation conditions, the same DC batch was used to stimulate naive CD4 T cells in a heterologous co-culture system. On day 6 of co-culture, we measured Th cell expansion fold (Exp Fold) and a total of 17 distinct Th cytokines broadly representing the spectrum of Th cell output responses (STAR Methods). In total, we produced a unique dataset of coupled measurements of DC-derived Th stimuli and Th response cytokines from 428 independent observations from 44 independent donors (Figure 1A; Table S2).

Variability and Specificity of DC Communication Signals

We asked whether our systematic DC stimulation strategy could generate important variations in the expression of individual DC-derived Th stimuli. All Th stimuli were expressed over at least three logs (Figure 1B) with high coefficients of variation (>0.44; Figure 1C). Interleukins had higher variability (10^4–10^5) and high coefficients of variation from 2.72 for interleukin-12 (IL-12) p70 (IL-12) to 1.43 for IL-6. CD11a had a wide expression range (10^4) but the smallest coefficient of variation (0.44), with values distributed around the mean (Figure 1C). Hence, we were able to generate highly variable expression patterns for all Th stimuli.

We sought to identify conserved and specific patterns of Th stimuli in response to standard DC perturbators. We compared the expression levels of DC-derived Th stimuli under three conditions belonging to distinct classes of microbes—LPS (100 ng/mL, bacteria), zymosan (10 μg/mL, fungi), and flu (1×, Viruses)—that were used across at least 17 MoDC biological replicates (Figure 1D). Medium MoDCs (negative control) expressed lower levels of activation-associated communication molecules (Figures 1D and S1B). We confirmed previous findings, validating our experimental system: (1) zymosan induced specifically IL-10 and IL-23, (2) flu induced a large amount of IL-28α, and (3) LPS and zymosan induced a large amount of IL-12 (Figures 1D and S1B). In addition, we identified novel specific inductions of DC-derived Th stimuli: zymosan-treated MoDCs expressed the highest levels of CD54 and PVR, flu-treated MoDCs specifically induced ICOSL, and LPS-treated MoDCs induced the highest levels of CD30L and CD83 (Figure 1D). Specificity of expression of a given signal for a given DC stimulation was determined using Wilcoxon statistical test (Figure S1B). Hence, standard DC perturbators induced specific patterns of Th stimuli.

Defining the Spectrum of DC Communication States

Next we aimed to assess the spectrum of DC communication states, as defined by their expression pattern of communication signals, across the 82 DC conditions. We computed the mean expression of biological replicates for each DC-derived Th stimulus and performed unsupervised hierarchical clustering to identify classes of the most similar conditions (C1–C82, y axis) and DC-derived Th stimuli (x axis) (Figure 2A). This revealed five groups of DC conditions (Figure 2B). Each of the four standard DC conditions (Figure 1D) belonged to a different group (Figure 2A).

Group 1 was defined by high expression of adhesion molecules such as CD18, ICAM-2, ICAM-3, and CD29 and low levels

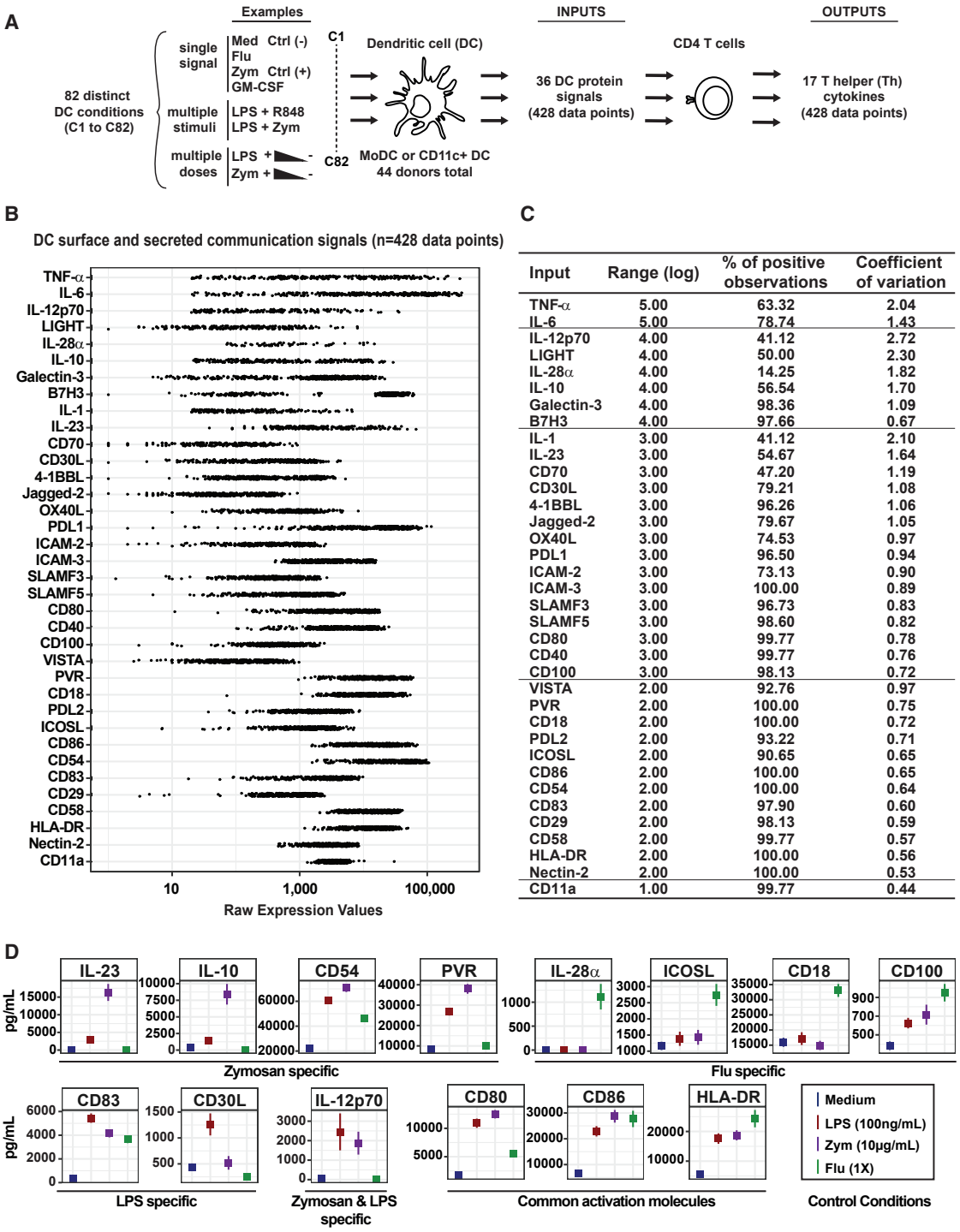

Input	Range (log)	% of positive observations	Coefficient of variation
TNF-α	5.00	63.32	2.04
IL-6	5.00	78.74	1.43
IL-12p70	4.00	41.12	2.72
LIGHT	4.00	50.00	2.30
IL-28α	4.00	14.25	1.82
IL-10	4.00	56.54	1.70
Galectin-3	4.00	98.36	1.09
B7H3	4.00	97.66	0.67
IL-1	3.00	41.12	2.10
IL-23	3.00	54.67	1.64
CD70	3.00	47.20	1.19
CD30L	3.00	79.21	1.08
4-1BBL	3.00	96.26	1.06
Jagged-2	3.00	79.67	1.05
OX40L	3.00	74.53	0.97
PDL1	3.00	96.50	0.94
ICAM-2	3.00	73.13	0.90
ICAM-3	3.00	100.00	0.89
SLAMF3	3.00	96.73	0.83
SLAMF5	3.00	98.60	0.82
CD80	3.00	99.77	0.78
CD40	3.00	99.77	0.76
CD100	3.00	98.13	0.72
VISTA	2.00	92.76	0.97
PVR	2.00	100.00	0.75
CD18	2.00	100.00	0.72
PDL2	2.00	93.22	0.71
ICOSL	2.00	90.65	0.65
CD86	2.00	100.00	0.65
CD54	2.00	100.00	0.64
CD83	2.00	97.90	0.60
CD29	2.00	98.13	0.59
CD58	2.00	99.77	0.57
HLA-DR	2.00	100.00	0.56
Nectin-2	2.00	100.00	0.53
CD11a	1.00	99.77	0.44

Figure 1. Variability and Specificity of DC Communication Signals

(A) Experimental strategy.

(B) Raw expression values of the 36 DC communication signals (n = 428 data points).

(C) Statistical descriptors of the 36 DC communication signals: expression range (log magnitude), percentage of positive observations among the 428 datapoints, and coefficient of variation.

(D) Average expression values and SD for the four indicated DC signals for MoDCs.

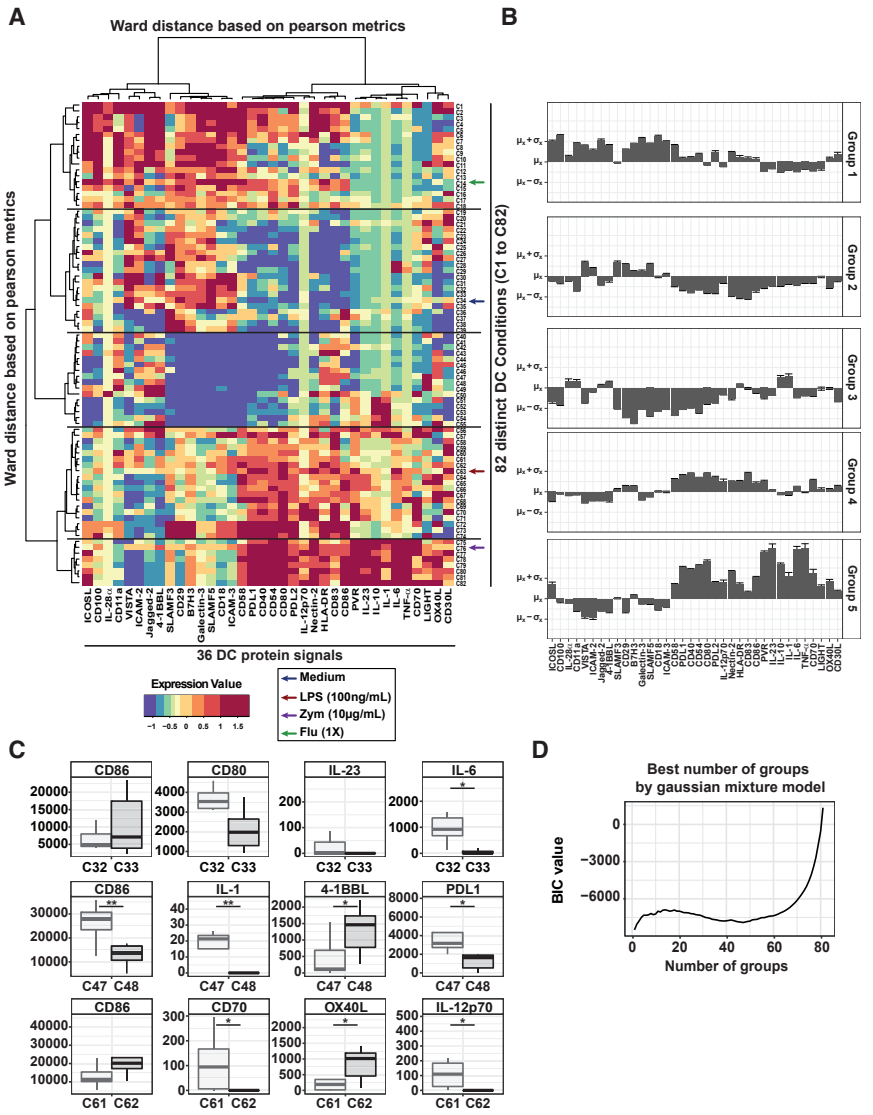

Figure 2. The Diversity of DC States Is Defined by Unique Combinations of Communication Molecules

(A) Heatmap showing expression values of each 36 DC-derived signal, performed with hierarchical clustering on Pearson metrics for the DC signals and Euclidian distances for the 82 DC conditions.

(B) Expression profiles (mean and SD) of the 36 communication molecules within the five groups of DC conditions, defined by hierarchical clustering. Expression data were logged and scaled so μ represents the mean and σ the SD of the expression of a given DC signal across the whole dataset.

(C) Boxplot of selected DC signals for pairs of stimulatory conditions defined as being the most correlated within our dataset by Pearson correlation (t test).

(D) Best number of groups by Gaussian mixture model, determined using the 428 points of the 36 DC parameters.

of co-stimulatory molecules and cytokines with the exception of high IL-28a. Group 2 showed low expression for most DC-derived Th stimuli but high levels of integrins, VISTA and B7H3, suggesting a capacity to interact with T cells and transmit co-inhibitory signals. Group 3 showed a complementary pattern, lack of group 1- and group 2-specific molecules, and intermediate or high levels of co-stimulatory molecules such as CD83, CD86, HLA-DR, 4-1BBL, and OX40L. This suggested potent T cell stimulating functions. Group 4 exhibited high levels of molecules from the B7 and TNF superfamilies, such as CD80, CD86, PDL1, PDL2, and CD40, but intermediate or low cytokine levels. In contrast, group 5 showed the highest level of cytokines and molecules of the B7 and TNF superfamilies (Figure 2B).

Next we sought to analyze intra-cluster heterogeneity. We selected three pairs of perturbators most closely related as defined by Euclidian distance (C32 [MoDC HKLM, MOI 1] and C33 [MoDC HKCA, MOI 1], C47 [bDC LPS, 100 ng/mL] and C48 [bDC HLKM, MOI 1], and C61 [MoDC R848, 1 µg/mL] and C62 [MoDC PAM3, 10 µg/mL]) and compared them regarding expression of the 36 DC-derived Th stimuli (Figure 2C). C32 and C33 did not exhibit significant differences in CD80 and CD86 expression, reflecting equal levels of DC activation. They were statistically different only for IL-6, with levels ranging from complete absence in C33 to over 1 ng/mL in C32 (Figure 2C). In contrast, the pairs C47/C48 and C61/C62 showed significant differences for multiple Th stimuli. C47 expressed significantly more CD86, PDL1, and IL-1 than C48. On the contrary, C48 expressed higher levels of 4-1BBL. C61 and C62 showed marked differences in CD70 and IL-12 (higher in C61) and OX40L (higher in C62) levels. Hence, each DC condition expressed unique combinations of DC-derived Th stimuli, suggesting different communication potential with CD4 T cells.

An unsupervised Gaussian mixture model showed that the highest Bayesian information criterion (BIC) value corresponded to 82 groups, confirming that each DC condition induced a unique profile of the 36 communication molecules (Figure 2D).

Using principal-component analysis (PCA), we showed that neither the date of the experiment nor the donor batch had a major effect on clustering (Figure S1C; STAR Methods).

The Heterogeneity of DC-Induced Th Cytokine Responses

We characterized the diversity of CD4 T cell output responses, as assessed by Th cytokine profiles, following co-culture of naive CD4 T cells with activated DCs across the 82 conditions described previously. Th cytokines exhibited important variations across the 428 observations (Figure 3A). Some cytokines, such as IL-2, TNF-α, GM-CSF, TNF-β, and IL-3, were always detected (Figure S2A).

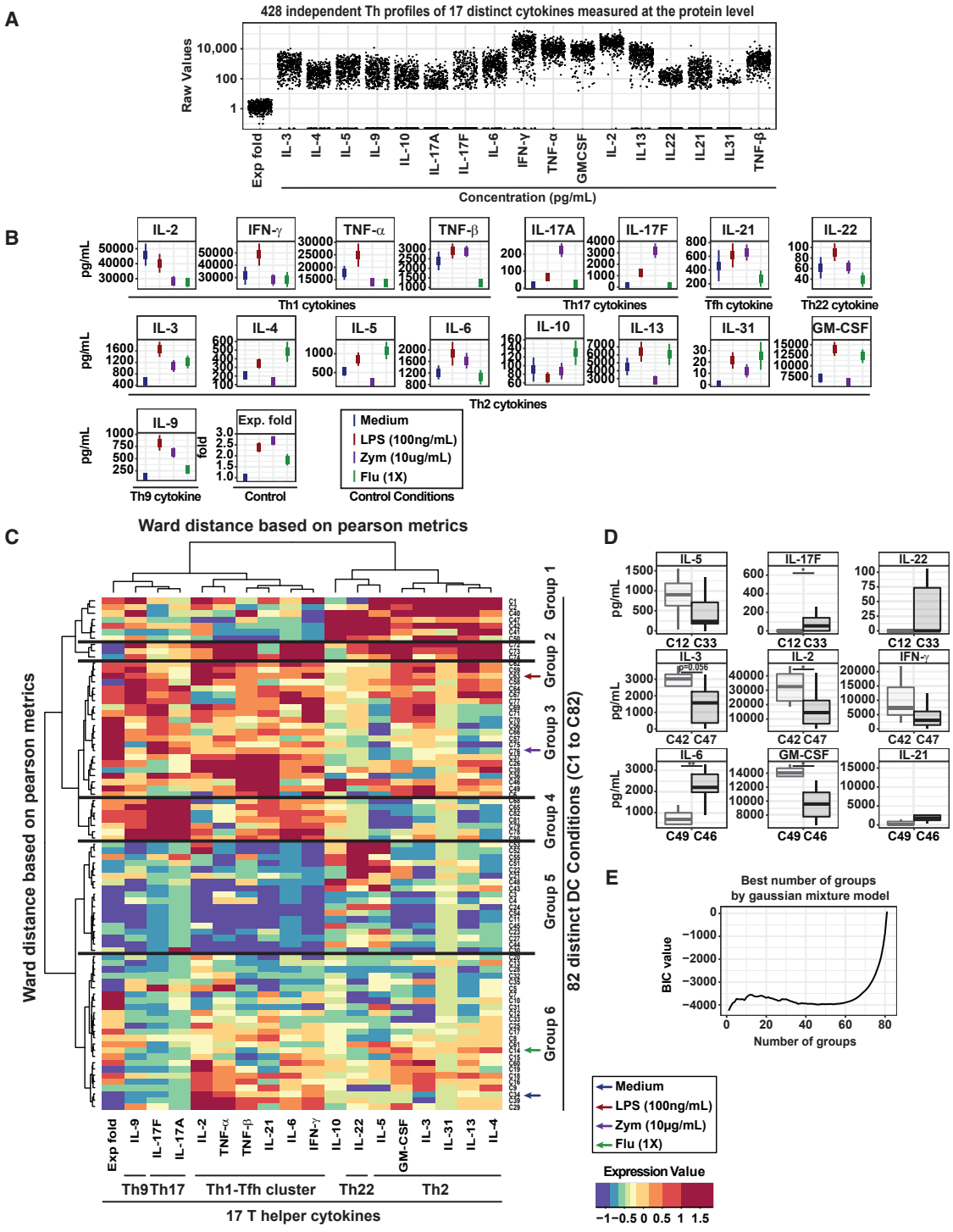

Figure 3. Th Cytokine Responses Mirror the Variability in DC Communication States

(A) Raw expression values of each of the 18 Th-derived parameters (n = 418 data points).

(B) Average expression values and SD for all Th-derived signals under the MoDC conditions medium, LPS, zymosan, and flu.

(C) Heatmap of expression values of each 18 Th parameters, performed with hierarchical clustering on Pearson metrics for the DC signals and Euclidian distances for the T cell conditions.

(D) Boxplot of Th signals for pairs of conditions selected as being the most correlated within our dataset by Pearson correlation (t test).

(E) Best number of groups by Gaussian mixture model, determined only using the 428 points of the 18 Th parameters.

To identify Th subset signatures, we compared cytokine expression under our four standard conditions: medium (negative control), LPS, zymosan, and flu. The Th17 cytokines IL-17A and IL-17F were induced predominantly in zymosan MoDCs. LPS MoDCs induced mixed Th1, Th2, and Th9 responses characterized by high IFN-γ, IL-13, IL-3, and IL-9 compared with medium. Flu MoDCs induced the Th2 cytokines IL-4, IL-5, and IL-31 (Figures 3B and S2B). These results indicate that, under the LPS, zymosan, and flu conditions, each DC state induced a distinct set of Th cytokine responses corresponding to prototypical Th signatures or mixed Th profiles.

Th Cytokine Responses Mirror the Variability in DC Communication States

We asked whether Th cytokine responses would reveal distinct patterns or a continuum of responses mirroring each of the DC communication states (Figure 2A). We performed hierarchical Pearson clustering on our 18 distinct Th-derived variables across the entire 82 DC-activating conditions (Figure 3C). This revealed 6 distinct groups, although intra-group heterogeneity was evident in almost all groups. Interestingly, DC perturbation conditions (C1–C82) did not appear in the same order compared with DC communication signal clustering (Figure 2A), indicating that closely related patterns of DC-derived Th stimuli did not necessarily induce the closest patterns in Th cytokine responses.

Group 1 was dominated by production of IL-10, IL-22, IL-5, GM-CSF, IL-3, IL-31, IL-13, and IL-4 (Figure S2C). Group 2 was the most heterogeneous and included the inflammatory cytokines TNF-α and IL-6 co-expressed with variable levels of the Th1 (IFN-γ) and Th2 (IL-4 and IL-13) cytokines (Figure S2C). Group 3 expressed IL-21, IFN-γ, and IL-17F but no or low IL-17A, suggesting the possibility of differential regulatory mechanisms (Figure S2C). Group 4 was dominated by the Th17 cytokines IL-17A and IL-17F, group 5 by IL-22, and group 6 by IL-2. Distinct sets of DC perturbation conditions and, hence, patterns of DC-derived communication molecules were associated with each of these groups (Figure 3C). This was the first suggestion of specific rules underlying input-output relationships in DC-Th communication.

Because of intra-group heterogeneity, we asked whether most correlated conditions within the same cluster would differ from each other (Figure 3D). C12 and C33 were associated to different levels in IL-17F, whereas C42 and C47 were different in IL-2 and C46 and C49 were different in IL-6 and GM-CSF levels (Figure 3D). As for the DC dataset, we found that 82 was the best number of groups in our Th-derived dataset, based on a Gaussian mixture model (Figure 3E). This suggested that a single DC profile of communication molecules would induce a unique set of Th cytokines.

A Data-Driven Lasso Penalized Regression Model Predicts Th Cytokine Responses from Combinations of DC-Derived Th Stimuli

Having generated distinct patterns of DC-derived communication signals associated with a diversity of induced CD4 T cell cytokine responses, the question of their relationship appeared to be critical to decipher DC-Th communication. Given the complexity of the dataset and the lack of clear hypotheses concerning the majority of DC-derived Th stimuli, we applied an unsupervised mathematical modeling strategy (Figure 4A).

The MultiVarSel strategy with stability selection performed similarly as the internal positive control and better than other methodologies tested (Figure S3A; STAR Methods). Therefore, we applied MultiVarSel to the modeling of our experimental data (Figure 4A). This methodology takes into account the dependencies that may exist among Th cell cytokines and combines Lasso criterion and stability selection to select associations between DC-derived signals (inputs) and Th cytokines (outputs) (STAR Methods).

Our multivariate model identified a large number of significant positive (red) and negative (blue) associations of the 36 DC-derived Th stimuli with the 17 Th-derived cytokines (Figure 4B). White squares represent the absence of significant association (Figure 4B). The frequency of selection obtained for each input-output association is provided in Figure S3B.

Our mathematical model revealed (1) the effect of each DC communication signal on Th output responses and (2) the critical regulators for each Th cytokine. For example, negative regulators of IL-10 were OX40L, 4-1BBL, IL-12, TNF-α, CD58, VISTA, Galectin-3, CD80, CD29, IL-1, ICAM-3, SLAMF3, IL-28α, and CD83, and positive regulators were Jagged-2, PDL1, IL-10, CD11a, HLA-DR, ICOSL, CD100, CD30L, CD18, ICAM-2, and CD86 (Figure 4B). Hence, the model can predict IL-10 production by responding Th cells for any DC, given the expression level of these molecules. It allows simulating loss or gain of function of an input. Similar insight can be obtained for each of the 17 Th cytokine responses, which may be explained by a combination of DC-derived communication signals.

We used computational cross-validation to evaluate the error of prediction of our model (Figure 4C). For all Th cytokines, the multivariate outperformed the best univariate model (Figure S3C). We ranked Th cytokines based on their prediction errors; the Th variables best explained by our model were IL-6, IL-17F, Exp Fold, and IL-3 (Figure 4C).

To address DC type specificity in model performance, we calculated the cross-validation error for each Th output of the MoDC and bDC dataset, respectively. Our model predicted equally well the majority of the outputs for the two DC types (Figure S3D). For a few outputs, mostly IL-22 and TNF-β, the model was more error prone in bDCs than MoDCs (Figure S3D). Interestingly, a higher prediction error was found for TNF-β in 5 of 118 observations (Figure S3E), where TNF-β levels were very high (range, 6.7–22.2). This suggested that a TNF-β-promoting input signal might be involved in those 5 cases but not included in our model. For IL-22, more observations had a higher prediction error in bDCs compared with MoDCs, but the prediction error range and distributions were similar, suggesting that the input-output relationship was conserved (Figure S3E).

We performed hierarchical clustering for both DC and T cell-derived variables to identify co-regulations between Th outputs. We retrieved relevant clusters of Th cytokines belonging classically to the same Th subset (Figure 4B). The Th2-related cytokines IL-13, IL-31, IL-5, IL-4, IL-10, and GM-CSF were found in the same cluster, suggesting that their induction would be controlled by similar mechanisms. IL-17A and IL-17F were also

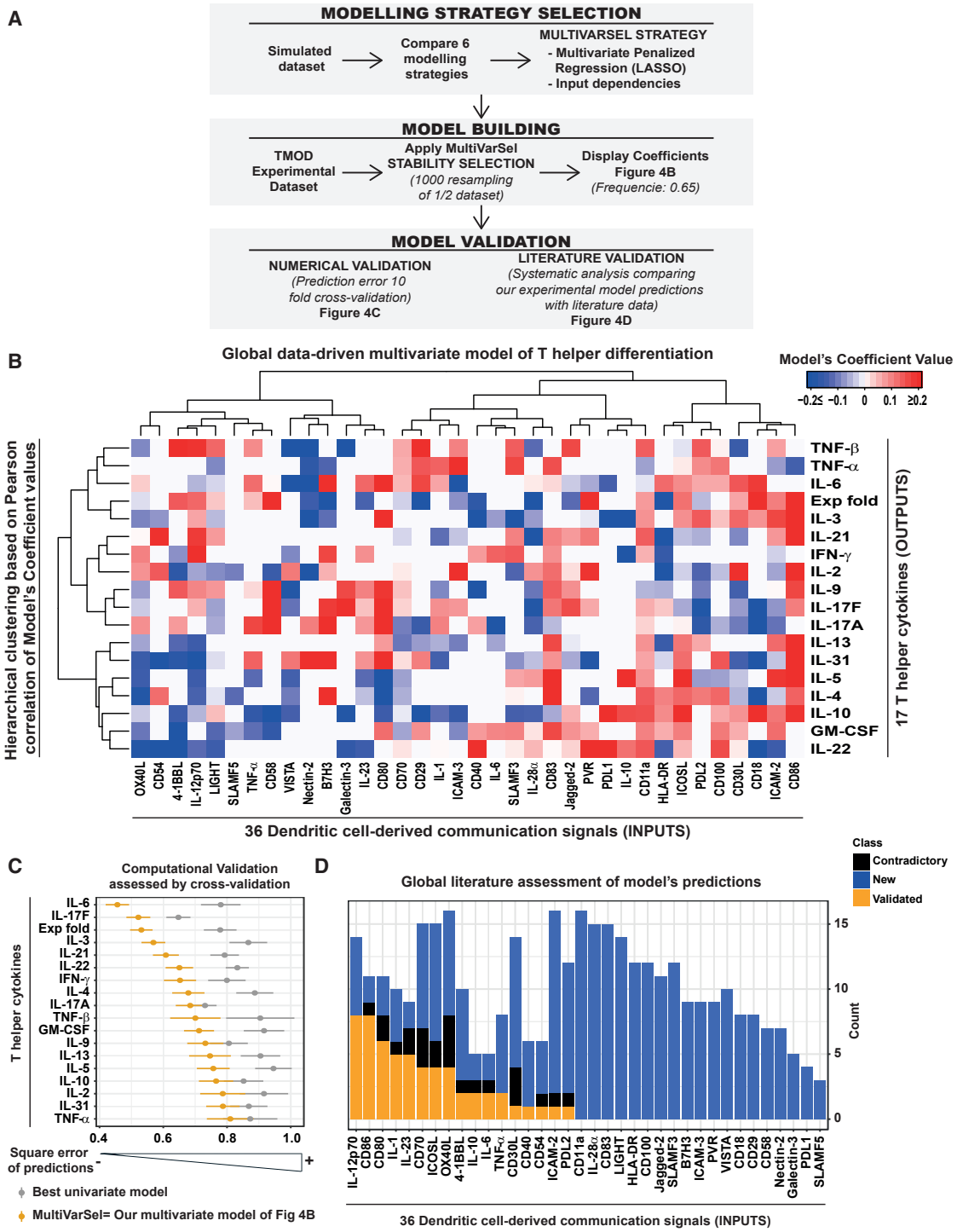

Figure 4. A Data-Driven Lasso Penalized Regression Model Predicts Th Differentiation Outcomes from DC-Derived Communication Signals

(A) Mathematical modeling strategy.

(B) Heatmap of the model's coefficient values of the MultiVarSel-derived model, explaining the 18 Th parameters based on the 36 DC-derived signals (Pearson correlation-based hierarchical clustering).

(C) Mean and SE of prediction error values obtained by 10-fold cross-validation for Th parameters using the multivariate model (yellow) and the best univariate model (gray) within the 36 DC signals.

(D) Literature-based validation score. For each DC signal, all predicted associations with Th cytokines were categorized as "new," "validated," or "contradictory."

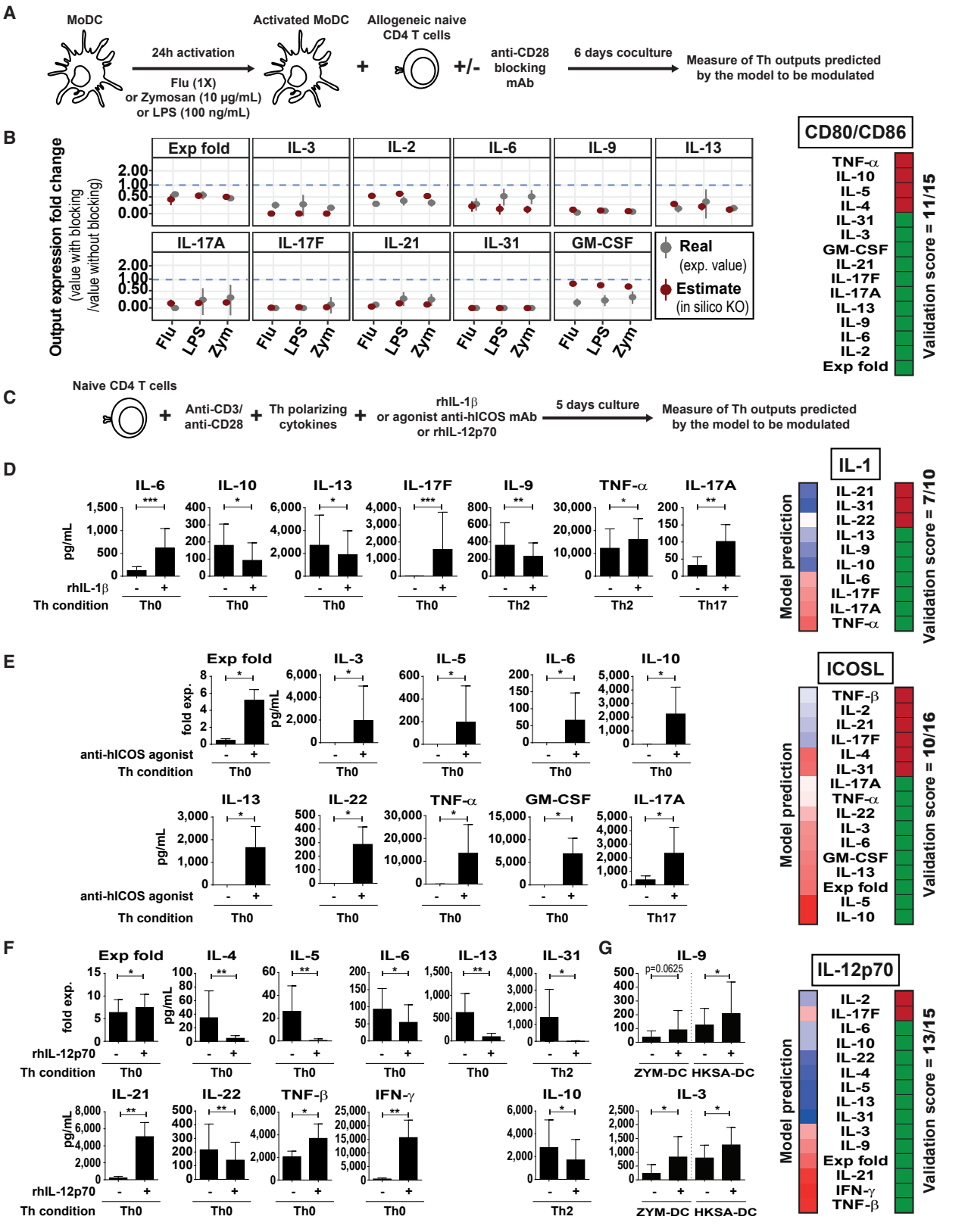

(legend on next page)

in the same cluster, implying that the model associated them with closely related DC communication signals (Figure 4B). Surprisingly, our model closely related IL-9 expression to IL-17A and IL-17F, suggesting common regulators. It also clustered IL-22 closer to the Th2 than to the Th17 cytokines. IL-21 was associated with the Th1 cytokines IL-2 and IFN-γ (Figure 4B).

The Multivariate DC-Th Model Reveals Novel Regulators of Th Cytokine Responses

We systematically compared our model results with the literature as a knowledge-based validation but also novelty assessment. We screened 178 relevant articles (STAR Methods) and extracted information regarding specific molecular control of a given Th cytokine by DC-derived signals measured in our model (Table S3). We computed a validation score based on the number of articles identifying the same associations than our model (STAR Methods). IL-12 ranked as the top DC communication signal for which our model predictions globally recapitulated existing knowledge (8 of 13 predicted associations). Among other known associations, IL-23 was positively associated with IL-17A and IL-17F, IL-10 was positively associated with IL-10 and negatively with IFN-γ, and CD40 was positively associated with IFN-γ.

However, the model also predicted 290 associations that were not described previously. Putative novel regulators were identified for all Th outputs (Table S4). The robustness of each prediction could be estimated by the value of the coefficient and by the frequency of detection of the association (Table S4). Examples of high scores were B7H3 and CD83 association with IL-4, 4-1BBL association with IL-9, ICOSL association with IL-13, and OX40L negative association with IL-22 (Table S4). Overall, literature knowledge was retrieved for 80 distinct input-output relationships presented in our model (Figure 4B); 56 were in agreement with our model, representing a global literature validation score of 70%.

Systematic and Independent Experimental Validation of Model's Predictions

We performed systematic experimental validation by selecting a subset of target inputs and systematically measuring the Th outputs selected by our model. We assessed the novelty of each validated prediction (Table S3).

First we addressed systematic validations of model predictions by blocking experiments (Figure 5A). We performed double *in silico* knockout for CD80 and CD86 under the three conditions—LPS (100 ng/mL), flu (1×), and zymosan (10 μg/mL) MoDCs—in which CD80 and CD86 were highly expressed and predicted an effect on 15 distinct Th outputs (Figure 5B), 11 of which were successfully experimentally validated (STAR Methods). The positive role of CD80 and CD86 on IL-3 and IL-31, to our knowledge, have not been described elsewhere. The predictions we failed to validate were for IL-4, IL-5, IL-10, and TNF-α (Figure S4A), all predicted to be decreased by CD80/CD86.

Then we validated the effects of three additional inputs: IL-1, ICOSL, and IL-12 used as exogenous factors (Figure 5C). First we gave the selected input together with anti CD3/CD28 signals (Th0) and systematically measured all Th outputs predicted by the model to be influenced by that input. In the absence of any effect, we gave the selected input under a Th2 (IL-4) or Th17 (IL-6, IL-1β, IL-23, and TGF-β) condition to detect additional synergistic or inhibitory effects required to validate the predicted effect. For example, it is not possible to validate the inhibition of a Th2 cytokine without significant production of this cytokine at baseline.

We focused on the ten predictions made by our model for IL-1 (Figure 5D). By adding IL-1β to the Th0 condition, we were able to detect significant upregulation of IL-6 and IL-17F and significant downregulation of IL-10 and IL-13. IL-10 downregulation and IL-6 upregulation were also significant in the Th2 context (Figure S4B). Under a Th2 condition, we validated significant upregulation of TNF-α and downregulation of IL-9 by IL-1β (Figure S4B), not seen in Th0 (Figure S4B). Under a Th17 condition, we observed a positive effect of IL-1β on IL-17A. We could not validate the predictions regarding IL-21, IL-31, and IL-22 (Figure S4B). In total, 7 of 10 predicted effects of IL-1 were validated. Interestingly, the positive role of IL-1β on induction of IL-6 by Th cells was not known (Table S3) and may suggest new biology and amplification loops in an inflammatory context.

We used a similar strategy to validate predictions regarding ICOSL using an anti-ICOS agonistic antibody. Overall, we validated 10 of 16 predictions (Figure 5E and S4C; STAR Methods). Interestingly, five of the 10 validated predictions were novel (Table S3; IL-5, IL-13, IL-3, GM-CSF, and IL-22), suggesting common pathways to induce IL-22 and Th2 responses.

Finally, we experimentally tested the predictions regarding IL-12 (Figure 5F). Adding IL-12 to the Th0 condition validated an induction of IFN-γ, IL-21, Exp Fold, and TFN-β. We also validated the inhibitory role of IL-12 on Th2 cytokine (IL-4, IL-5, and IL-13), IL-6, and IL-22 production. Using the Th2 condition, we further validated the inhibitory role of IL-12 on IL-10 and IL-31. The effects of IL-12 on TNF-β, IL-31, and IL-6 have not been described previously (Table S3).

Because our anti-CD3/CD28 system did not allow validating IL-12 effects on IL-2, IL-17F, IL-3, and IL-9 (Figure S4D), we wondered whether DC-dependent factors could affect the role

Figure 5. Independent and Systematic Experimental Validation of the Model's Prediction

(A) CD28 blocking experimental design in DC-T co-culture.

(B) Comparison of the predicted versus observed fold change following CD28 blocking; n = 6 donors.

(C) Experimental scheme of the "adding" validation procedure used in (D)–(F).

(D) DC-free validation experiment studying the effect of adding IL-1β in Th0, Th2, and Th17. Naive T cells were stimulated by anti-CD3/CD28 beads; n = 6 donors.

(E) DC-free validation experiment studying the effect of adding ICOS in Th0 and Th17. Naive T cells were stimulated by coated anti-CD3 and ICOS antibodies and soluble anti-CD28; n = 6 donors.

(F) IL-12 validation experiments in the DC-free system. Naive T cells were stimulated by anti-CD3/CD28 beads under Th0 and Th2 conditions; n = 8 donors.

(G) Validation of IL-12 predictions regarding IL-3 and IL-9. bDCs were cultured with naive CD4 T cells. IL-12 at 10 ng/mL was added for 6 days; n = 6 donors.

For (B) and (D)–(G), each panel shows the mean and SD of cytokine concentration, measured on restimulated Th supernatants (Wilcoxon test).

of IL-12 on these cytokines. We selected DC conditions with very low production of IL-12 (C51 and C55; Figure 2A) and performed a co-culture with naive T cells, adding or not adding IL-12. As a positive control, IL-12 was able to induce IFN-γ in both zymosan and HKSA conditions (Figure S4E). We did not validate the role of IL-12 on IL-2 or IL-17F regulation (data not shown). However, we validated that IL-3 was induced by IL-12 in both zymosan DCs (C51) and HKSA DCs (C54) (Figure 5G), whereas IL-9 was significantly upregulated only in HKSA DCs. Overall, we were able to experimentally validate 13 of 15 predictions regarding IL-12.

Our systematic strategy established a validated prediction of the input-output relationship in 41 of 56 cases (73.2%), 13 representing new mechanisms identified by the model. This number is similar to or higher than the computational cross-validation (Figure 4C). Predictions with higher stability selection frequencies were more validated than those with low stability selection (Figure S4F). However, the value of the model's coefficients was not statistically different between the two groups (Figure S4F), indicating that the model efficiently captured associations with low coefficient values.

Although IL-12 was the input best explained by our model, we could not validate the predicted association between IL-12 and IL-17F (Figure S4D), neither in the literature nor in our systematic experimental validation. Previous studies have shown either no effect (Volpe et al., 2008) or a negative effect (Acosta-Rodriguez et al., 2007) of IL-12 on Th17 differentiation. We hypothesized that context-dependent effects may lead to new functions of IL-12, not accomplished by IL-12 as a single agent.

A Context-Dependent Model Reveals a Role of IL-12 in Th17 Differentiation

We designed a strategy to capture context-dependent effects of one input on any given output by integrating new composite variables into the model (Figure 6A). These new input variables were based on the co-occurrence of a given input with other DC-derived communication signals (i.e., contexts). They adopted the value of the given input (for instance, IL-12) in each observation where the co-expressed DC signal was present, and they took a zero value when the co-signal was absent. We could derive 455 context-dependent variables.

The model including all context-dependent variables performed less well (higher error of prediction) than our classical MultiVarSel strategy (Figure S5A), most likely because of overfitting issues dependent on the dataset size, with a number of input variables exceeding the number of data points used to fit the model. Therefore, we derived 36 models, each one integrating the context dependencies of one input (Table S5). For each of these models, we reported the coefficient and the stability selection frequencies of each input (Table S5). To globally estimate the influence of context dependencies within our data, we quantified the number of times an input variable was selected, either "alone" or "with" another one. We derived percentages of context dependencies and represented the results either per input (Figure S5B) or per output (Figure S5C). The inputs most likely to present "context-dependent" functions were PDL1 and SLAMF3, whereas CD11a and CD70 were mostly context-independent (Figure S5B). When analyzing the outputs, the models revealed that all cytokines could be regulated by context-dependent mechanisms with relatively similar percentages (range, 0.13–0.22) (Figure S5C).

We used this strategy to explain the role of IL-12 in the control of Th17 differentiation through identification of context-dependent effects. We found that adding context-dependent variables for IL-12 improved the model predictions for IL-17F and performed equally well for IL-17A (Figure 6B). We then focused on DC-derived signals that were kept significant by the model and observed distinct associations of the new IL-12 context-dependent variables with IL-17A and IL-17F (Figure 6C), including some differentially associated with IL-17A and IL-17F, respectively. Among various contexts, we found that IL-12 in the context of IL-1, ICAM-2, or Jagged-2 was associated with IL-17F, whereas IL-12 in the context of CD70, IL-23, or LIGHT was associated with IL-17A.

As a first level of *in silico* validation, we selected a DC condition under which IL-12 was co-expressed with many of these contexts, and DC-derived signals induced IL-17A and IL-17F by responder Th cells. Zymosan (10 μg/mL) on MoDCs fulfilled these criteria (Figures 1D and 3C). To study the specific effects of IL-12 in the context of all other DC communication signals induced by zymosan, we performed *in silico* IL-12 knockout in the IL-12 context-dependent model. We compared predicted values for IL-17A and IL-17F when IL-12 was kept or not kept in the model (Figure 6D). *In silico* knockout of IL-12 diminished the production of both IL-17A and IL-17F under the zymosan (10 μg/mL) condition. As experimental validation, we performed independent DC/T cell co-culture experiments using MoDCs treated with 10 μg/mL zymosan in the presence and absence of IL-12-neutralizing antibody (Figure 6E). Blocking IL-12 significantly decreased the production of IL-17A and IL-17F, as predicted (Figure 6E), and inhibited IFN-γ production (Figure S5D). The same model predicted no effect of blocking IL-12 in Curdlan MoDCs (Figure S5E), which we validated experimentally (Figure S5F).

Synergistic Interaction between IL-12 and IL-1 Explains Induction of IL-17F without IL-17A

Our model predicted distinct roles of IL-12 on IL-17A and IL-17F production depending on the context in which IL-12 is expressed. Interestingly, IL-12, IL-1, and CD80 were the top variables almost systematically selected by the model to explain the differences between IL-17A and IL-17F (Figure 7A). This corroborated the results in Figure 6C, where we found that IL-12 in the context of IL-1 was associated with IL-17F but not IL-17A. The model estimate for a stability selection of less than 0.8 indicated that IL-12, IL-1, and CD80 were positive contributors to the differences between IL-17A and IL-17F (Figure S6A). Consequently, we hypothesized that the combination of IL-12 with IL-1 would induce IL-17F independent of IL-17A.

To experimentally validate our hypothesis, we used a DC-free Th polarization assay, allowing us to specifically study the interaction between IL-12 and IL-1 regardless of any other molecular context. Naive CD4 T cells were polyclonally activated with anti-CD3/CD28 beads and put in distinct cytokine treatments: Th0 (no cytokine) and Th2 (IL-4) as negative controls; Th17 (IL-1β+IL-23+IL-6+TGF-β) as a positive control, IL-12, IL-1β, and IL-12+IL-1β. IL-12 alone induced IFN-γ and IL-21 and inhibited Th2-related cytokines, as expected (Figure S6B). IL-12 alone induced neither IL-17F nor IL-17A, but combining IL-12

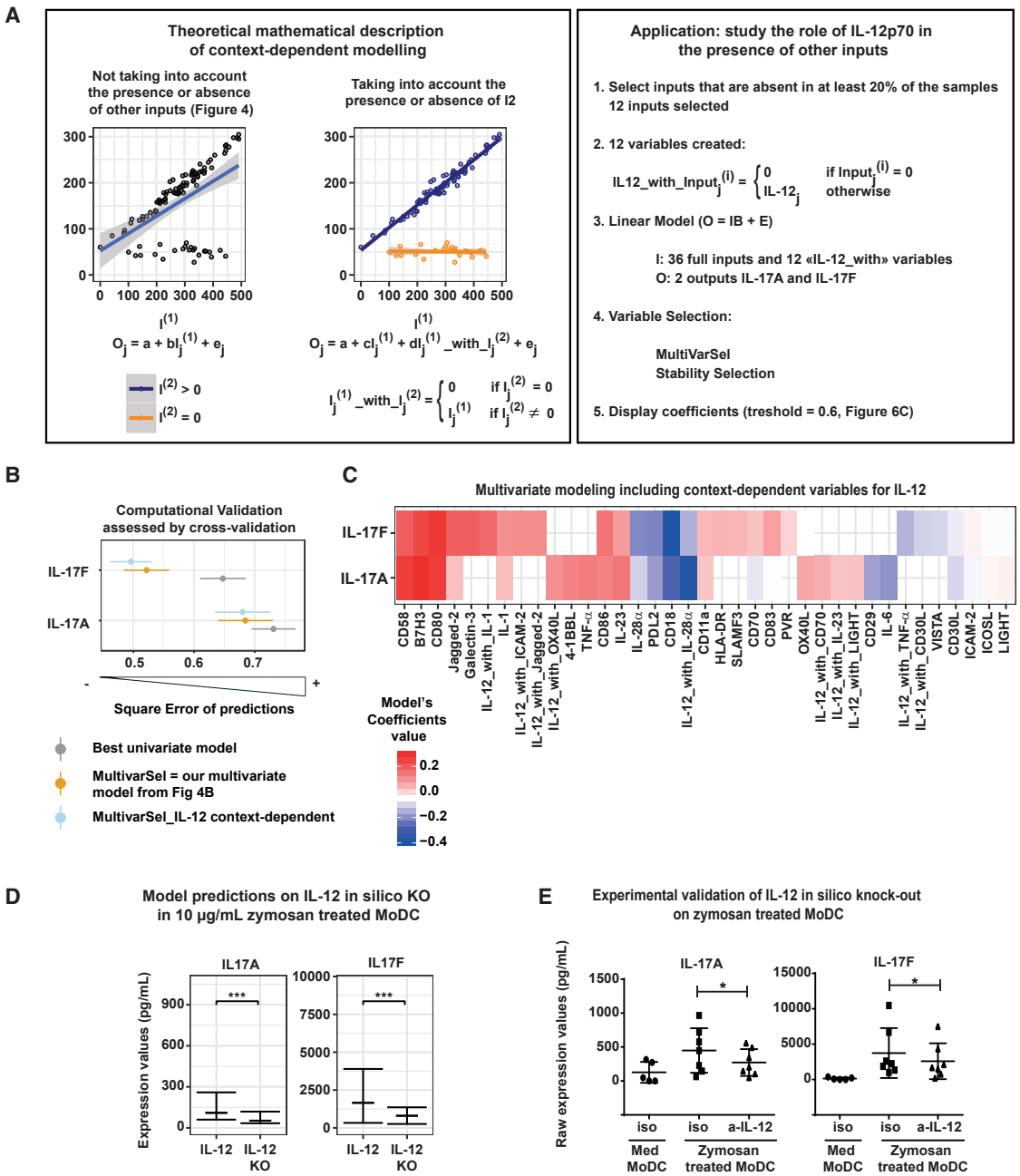

Figure 6. A Context-Dependent Model Reveals a Role of IL-12 in Th17 Differentiation

(A) Context-dependent modeling and application to IL-12. I, input; O, output.

(B) Error of prediction values obtained by 10-fold cross-validation for IL-17A and IL-17F, comparing the best univariate model (gray), MultiVarSel (yellow), and MultiVarSel with context dependencies (blue).

(C) Heatmap of the model's coefficient value of the context-dependent multivariate model explaining IL-17A and IL-17F.

(D) Model predictions regarding IL-12 *in silico* knockout (KO) under the zymosan MoDC condition for IL-17A and IL-17F values (blue) compared with experimental values in the presence of IL-12 (yellow); paired t test.

(E) Concentrations of IL-17A and IL-17F produced by Th cells after differentiation with zymosan MoDCs in the presence of anti-IL-12 neutralizing antibody or a matched isotype; n = 6 donors, paired t test.

with IL-1β dramatically induced IL-17F at levels comparable with the positive control, without a detectable amount of IL-17A, which fully validated the model predictions (Figure 7B).

This effect was specific to the IL-12+IL-1β combination IL-6, IL-23, or TGF-β alone or combined with IL-12 could not induce IL-17F expression (Figure S6C). The exact same pattern of Th

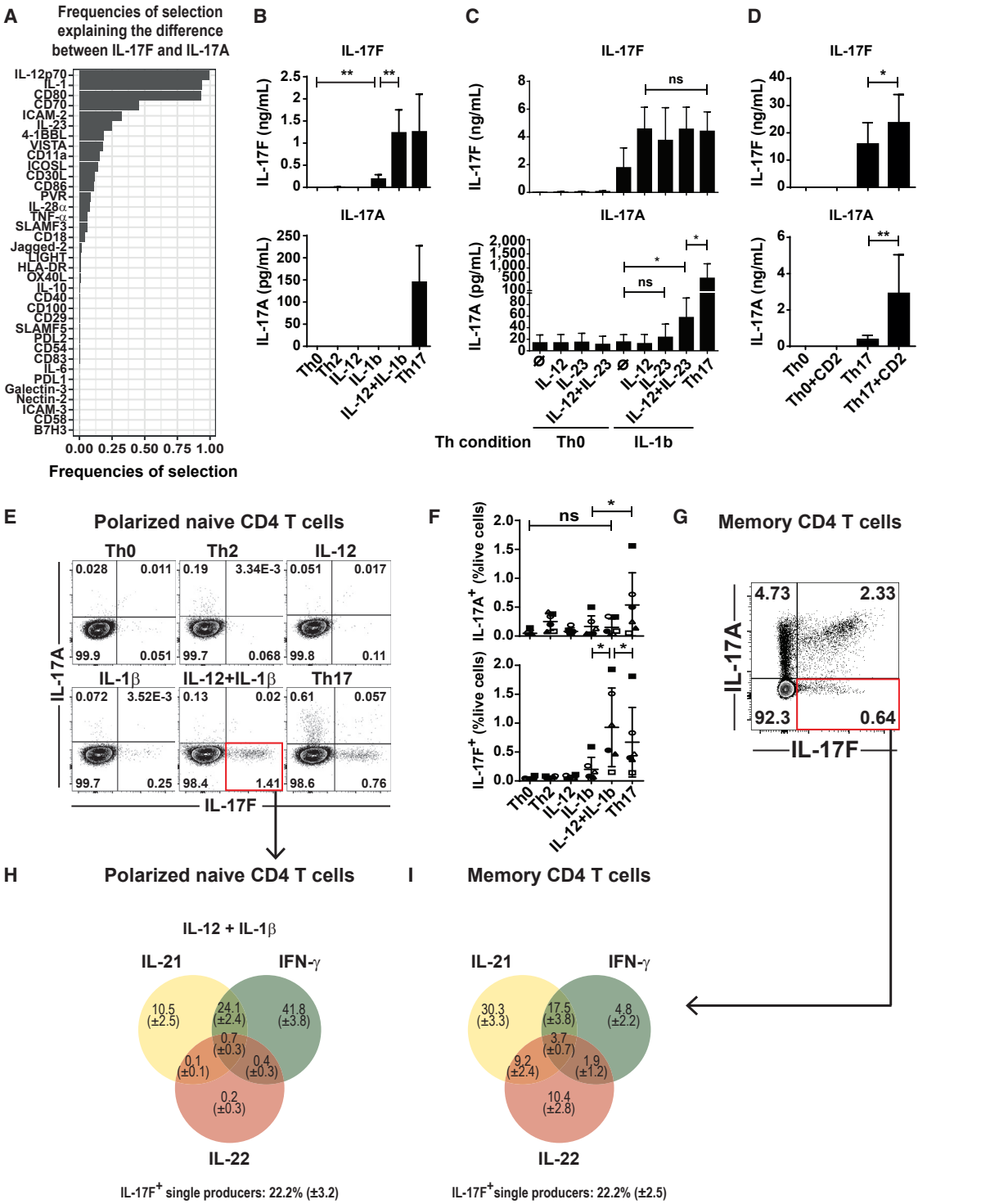

Figure 7. Synergistic Interaction of IL-12 and IL-1 Promotes IL-17F without IL-17A

(A) Stability selection frequencies of the different DC signals by a multivariate model, explaining the difference between IL-17F and IL-17A.

(B) Concentration of cytokines measured on restimulated Th supernatants. Naive CD4 T cells were differentiated for 5 days with anti-CD3/CD28 beads under the indicated conditions; n = 6 donors, paired t test.

(C) The same experimental design as in (B), with conditions as annotated; n = 6 donors, Wilcoxon test.

(D) Coated anti-CD2 and anti-CD3 together with soluble anti-CD28 were given for 5 days to naive CD4 T cells under Th0 or Th17 conditions. Cytokine concentrations were measured after 24-h restimulation on day 5. Mean and SD are shown; n = 8, Wilcoxon test.

(legend continued on next page)

cytokine expression was obtained by combining IL-1α or IL-1β with IL-12, which fit model predictions because those two variables were highly correlated (Figure S6D). The capacity of IL-12+IL-1β to induce IL-17F was resistant to the presence of other Th differentiation factors, such as IL-4 (Figure S6E). Using CellTrace Violet (CTV; Figure S6F), we could show that the production of IL-17F could not be attributed to the distinct proliferation capacity of Th cells under the IL-12+IL-1β condition.

Next we questioned whether Th cells generated under the IL-12+IL-1β condition would express transcription factors classically associated with Th17 differentiation. We measured 63 RNA transcripts by qPCR under Th0, Th2, IL-1β, IL-12, IL-12+IL-1β, and Th17 conditions (Table S6). The 63 genes included master regulators of the Th1 and Th2 subsets, such as T-bet and GATA3, respectively, and Th17 regulators, such as RORc, STAT3, BATF, and SATB1 (Ciofani et al., 2012). IL-17A and IL-17F regulation at the mRNA level mirrored the protein level (Figure S6H). IL-12+IL-1β induced significantly more RORc, BATF, and Bcl6 than IL-12 or IL-1β alone (Figure S6H), which could explain the induction of IL-17F and IL-21. Still, the levels of RORc and Bcl6 were lower in IL-12+IL-1β than under the Th17 condition (Figure S6H). T-bet was highly induced in IL-12+IL-1β in comparison with the IL-12 or Th17 conditions, indicating that Th1 differentiation was maintained and that T-bet did not inhibit IL-17F production. IL-12Rb2, a Th1 marker, was downregulated by IL-1β when added to IL-12, whereas IL-12, IL-12+IL-1β, and Th17 conditions all induced the IL-23 receptor (Figure S6H). SATB1 was specifically upregulated in IL-12+IL-1β in comparison with Th17 or IL-1β alone (Figure S6H), suggesting that it could play a role in the specific upregulation of IL-17F.

To globally assess the expression of the various Th lineage-specific factors, across IL-12- and IL-1-containing conditions, we performed a principal-component analysis (PCA) including all 63 mRNA variables (Figure S7A). Cells from the IL-12+IL-1β condition had an intermediate expression pattern between the IL-12 (Th1) and Th17 conditions. By decomposing the PCA space into vectors for each variable, we found that IL-17F, IL-23R, ICOS, and T-bet projected predominantly along the IL-12+IL-1β condition (Figure S7B), again pointing to mixed Th1/Th17 features.

We then addressed the link between IL-12 and IL-17A in various contexts. IL-12 with IL-23 was predicted to induce IL-17A but not IL-17F (Figure 6C). In a DC-free Th polarization assay, we used IL-12, IL-23, or IL-12+IL-23 and found that none of these conditions induced IL-17A (Figure 7C). We hypothesized that a third input could explain the positive link between "IL-12_with_IL-23" and IL-17A. Using an unsupervised analysis, we found IL-1 as a top variable with the highest correlation (Figure S7C). In addition, IL-12 and IL-17A positive correlation was significant specifically in the group of data points where IL-23 and IL-1 were expressed (Figures S7D and S7E) and was lost when only IL-1 or IL-23 was expressed with IL-12 (Figure S7D). Therefore, we tested whether IL-12+IL-23 would induce IL-17A in the presence of IL-1β. We validated a significant induction of IL-17A with no effect on IL-17F when IL-12 and IL-23 were given in the presence of IL-1β compared with IL-12 or IL-23 (Figure 7C). We measured IL-17A and IL-17F by qPCR and retrieved the same induction pattern (Figure S7F). Last, we could show that RORc was higher in IL-12+IL-23+IL-1β than in IL-12+IL-1β (Figure S7F).

Finally, we observed that our modeling strategy always identified CD58 as a main Th17 inducer because it positively affected both IL-17A and IL-17F (Figures 4B and 6C), an association that we had not seen during our systematic literature review (Figure 4D; Table S3). To test this hypothesis, we used an agonist anti-CD2 antibody that mimics the presence of CD58 (STAR Methods). As predicted, IL-17A and IL-17F were not induced by anti-CD2 alone under the Th0 condition. However, anti-CD2 significantly induced production of IL-17A and IL-17F under Th17 conditions (Figure 7D), which was confirmed by intracellular FACS staining (Figures S7H and S7I), with IL-17F upregulation restricted to IL-17A-positive cells (Figure S7I).

To establish the cytokine co-expression profiles of IL-12+IL-1β-treated Th cells at the single-cell level, we performed intracellular cytokine staining (Figure 7E). We confirmed that IL-12+IL-1β induced significantly more IL-17F-positive Th cells without co-production of IL-17A (Figure 7F). In naive CD4 T cells polarized with the Th17 cytokine cocktail (IL-1β, IL-6, TGF-β, and IL-23) we mainly found two subsets of Th17 cells producing either IL-17A or IL-17F, with very few cells co-producing both cytokines. To check for *in vivo* existence of those IL-17A and IL-17F single producers, we analyzed the human CD4 T cell memory compartment by intracellular FACS in healthy donor peripheral blood mononuclear cells (PBMCs). We could identify a small fraction of Th cells expressing only IL-17F in the absence of IL-17A, suggesting that this phenotype constitutes a differentiation endpoint (Figure 7G).

To gain more insight into the functional properties of these "Th17F" cells, we studied their co-production with IL-21, IFN-γ, and IL-22, all relevant to the Th17 and/or IL-12 pathways, *in vitro* (Figure S7J) and *ex vivo* (Figure S7K). Among IL-17F$^+$IL-17A$^-$ cells generated with IL-12 and IL-1β, the majority co-produced IFN-γ (41.8%), IL-21 (10.5%), or both (24.1%) (Figure 7H), reflecting a dominant role of IL-12. IL-17F$^+$/IL-17A$^-$ memory CD4 cells preferentially co-expressed IL-21 (30.3%) and IL-21 together with IFN-γ (17.5%) (Figure 7I), which matched the *in vitro* differentiated CD4 T cells. In addition, the percentage of IL-17F$^+$/IL-17A$^-$/IL-22$^-$/IL-21$^-$/IFN-γ$^-$ cells between *in vitro* IL-12+IL-1β stimulation and the *ex vivo* restimulated memory

(E) Day 5 intracellular FACS analysis of Th cells differentiated as in (B). Dot plots show a representative donor.
(F) Quantification of live total CD4 T cells producing either IL-17A or IL-17F; n = 6 donors, paired t test.
(G) Representative donor of CD4 memory T cells with intracellular FACS staining for IL-17A versus IL-17F.
(H) Venn Diagrams of IL-17F$^+$/IL17A$^-$ Th cells co-producing IL-22, IFN-γ, and IL-21 of naive CD4 T cells under the IL-12+IL-1β. IL-12+IL; mean percentage and confidence interval, n = 6 donors.
(I) Venn Diagrams of IL-17F$^+$/IL17A$^-$ Th cells co-producing IL-22, IFN-γ, and IL-21 of memory CD4 T cells stimulated for 5 h with PMA and ionomycin; mean percentage of 6 donors with confidence interval.

compartment was similar (22.2%), which indirectly supported that IL-12+IL-1β induced the emergence of IL-17F single producers.

Taken together, our results demonstrate a synergy between IL-12 and IL-1 in inducing IL-17F single-producing Th cells with possible physiopathological relevance.

DISCUSSION

Cell-cell communication may involve several tens of communication signals functioning concomitantly and possibly interacting with each other. These signals, in turn, modify many molecular and functional parameters in target cells. Such complexity cannot be captured and formalized without an integrated mathematical modeling approach. Theoretical models of Th cell differentiation have already been established (Abou-Jaoudé et al., 2015; Naldi et al., 2010) and include a large number of possible inputs to T cells. However, they suffer from three limitations: (1) they include input signals that may be expressed by diverse cell types in different anatomical locations; (2) they do not recapitulate combinations of input signals in their naturally occurring patterns and concentrations; and (3) they use prior knowledge to infer input-output relationships, which does not integrate possible context-dependencies and interactions. In parallel, data-driven models have been developed in response to predefined stimuli, such as Th17 (Yosef et al., 2013) or Th1/Th2 (Antebi et al., 2013), which do not recapitulate the integration of multiple communication signals. In our study, we applied an unbiased data-driven approach specifically designed to model DC-Th communication. Combinations and concentrations of input communication signals were measured as naturally determined by their intrinsic biological regulation. Subsequently, the input-output relationships were learned from the experimental data and integrated into any underlying context dependency and interaction, even when not described previously. This maximizes the relevance of the model and the potential for novel discoveries.

Cells can change state in response to environmental cues, a concept defined as plasticity (da Silva-Diz et al., 2018; Liu et al., 2001). Each cell state may be associated with different communication potential; i.e., different expression patterns of communication signals (Soumelis et al., 2002; Wang et al., 2014). To broadly cover the possible DC states, we used various DC-stimulatory conditions (cytokines, viruses, bacteria, fungi) at various doses and combinations and across a large number of observations (>400). This prevented us from biasing our observations toward certain quantitatively or qualitatively extreme behaviors. After the model has learned the rules from such an extended range of observations, we anticipate that it should be able to predict behaviors in situations not necessarily covered in our original dataset, as confirmed in our computational and experimental validations. This opens possibilities of application in many areas of immunology, inflammation, and immunotherapy.

RNA sequencing (RNA-seq) has offered a means of capturing the expression of many communication signals and their receptors to infer cell-cell communication between various cell types (Vento-Tormo et al., 2018). However, the RNA-to-protein correlation can be rather low (Liu et al., 2016) and varies a lot depending on the gene (Edfors et al., 2016). Consequently, RNA copies of a gene cannot be associated with a given functional output, preventing quantitative mathematical modeling. Functional response in target cells can only be estimated indirectly through surrogate activation markers, which is most often not performed. In our approach, all measurements of communication signals and output variables were done at the protein level, hence directly measuring the bioactive communication molecules with a direct link to a specific response in target cells. This ensures robustness of the modeling strategy, as evidenced by our model's ability to recapitulate most of the known relationships in DC-Th cell communication.

Modeling complex biological behaviors in a quantitative manner is challenging. In data-driven models, it relies in large parts on the choice of explanatory (input) variables, which drive the induction or regulation of output variables. Here we selected DC-derived communication molecules through exhaustive literature mining. The model was able to integrate 36 input and 18 output variables in a quantitative manner, which makes it a reference in the field. We have been able to describe patterns of DC communication molecules in a way that goes beyond the classical view of immature versus mature DCs (Banchereau and Steinman, 1998; Guermonprez et al., 2002). In fact, we showed that almost every DC stimulatory condition leads to a distinct DC state. This is a first step in defining general combinatorial rules of DC-derived communication molecules: co-expressed molecules form the basis of putative context-dependent effects. Through the large number of variables handled by the model, we identified 290 novel associations explaining major immunoregulatory cytokines, which may lead to the discovery of novel functions of known DC molecules and suggest novel therapeutic targets.

Going further into the complexity of communication, we explored context dependencies of communication signals. In verbal communication, the context may dramatically alter the meaning of an individual word. Currently, there is no systematic way to search for context dependencies in biological communication. In our modeling strategy, we devised a method that introduces context-dependent variables for a given molecule. This allows unbiased identification of context-dependent functions that would have been missed by classical regression models. For example, we identified a new function for IL-12 in promoting IL-17F production by Th cells, which was completely unexpected based on prior knowledge (Korn et al., 2009). Identifying such context dependencies before therapeutic targeting of a DC-Th communication molecule may improve the prediction of its effect.

Given that DC-Th communication is central to a large number of physiopathological conditions (Keller, 2001), we can foresee multiple applications for the model. Based on expression pattern of DC molecules, the model can predict the induced Th cytokine profile. Quantitative measurements of DC communication molecules in a given disease or in an individual patient *ex vivo* can be used to simulate the corresponding Th response. Depending on the outcome, strategies may be devised to re-orient the response toward a protective or less pathogenic profile, again through model-based predictions. Alternatively, starting from a Th profile (cytokine or groups of cytokines), the appropriate molecular targets can be manipulated through gain- or loss-of-function experiments to amplify or inhibit a given Th cytokine. Last, the model can help predict the most appropriate vaccine adjuvant to obtain

protective immunity against some microbes or to re-orient a pathogenic Th response. For example, all DC molecules positively associated in the model to Th2 responses are potential targets to decrease pathogenic Th2 allergic inflammation (Ito et al., 2005; Nakayama et al., 2017; Soumelis et al., 2002).

Using DC-Th communication as a model, we established a framework that can now be applied to other types of cell-cell communication following 5 major steps: (1) systematic perturbation of the "sender" cell to generate a diversity of communication states; (2) broad, quantitative, and protein-level measurement of communication molecules relevant to the sender cell; (3) systematic quantitative assessment of the response in "receiver" or target cells; (4) MultiVarSel modeling of the input-output relationship, which defines communication rules; (5) *in silico* and experimental validation. Currently, we believe that cell type specificities in expression of communication molecules and in their function would prevent us from generalizing our DC-Th model to other cell types. Comparing different quantitative models of cell-cell communication will ultimately tell us whether cells speak the same language (i.e., whether they express similar patterns of communication molecules) and whether the same communication molecule has the same meaning (function) when expressed by two different cell types.

STAR★METHODS

Detailed methods are provided in the online version of this paper and include the following:

- KEY RESOURCES TABLE
- LEAD CONTACT AND MATERIALS AVAILABILITY
- EXPERIMENTAL MODEL AND SUBJECT DETAILS
  - Human subjects
- METHOD DETAILS
  - PBMCs purification
  - MoDC generation and activation
  - Blood dendritic cells purification
  - $CD4^+$ T lymphocytes purification
  - Paired protein measurement in DC/T coculture
  - IL-12 blocking experiment
  - CD28 blocking experiment
  - Addition of rhIL-12p70 during DC/T coculture
  - DC-free Th cell polarization
  - ICOS agonism
  - CD2 agonism
  - Flow cytometry analysis
  - Cytokine quantification
  - Gene expression quantification
  - Anti-human ICOS monoclonal blocking antibody
- QUANTIFICATION AND STATISTICAL ANALYSIS
  - Dataset quality control – batch effect
  - Dataset quality control – T cell expansion
  - Statistical tests
  - Statistical analysis
  - Model comparison and ROC Curves
  - Modeling strategy
  - Systematic literature review
- DATA AND CODE AVAILABILITY

SUPPLEMENTAL INFORMATION

Supplemental Information can be found online at https://doi.org/10.1016/j.cell.2019.09.012.

ACKNOWLEDGMENTS

We thank the Institut Curie Cytometry platform for cell sorting, P. Gestraud and F. Coffin for advice regarding statistical analyses, and O. Lantz and N. Manel for important discussions. We wish to thank L. Pattarini, B. Fould, W. Cohen, O. Geneste, B. Lockhart, V. Blanc, and their teams from the Institut de Recherche Servier for having produced and generously shared the anti-ICOS antibody. This work was supported by funding from Agence Nationale de la Recherche: ANR-16-CE15-0024-01, ANR-10-IDEX-0001-02 PSL*, ANR-11-LABX-0043 and ANR-17-CE14-0025-02 from Center of Clinical Inverstigation IGR-Curie: CIC IGR-Curie 1428 and from Ligue contre le Cancer: EL2016.LNCC/VaS. M.G. was funded by ANRS and ARC.

AUTHOR CONTRIBUTIONS

M.G., C.T., L.K., C.C., and P.S. performed the experiments. M.G. and V.S. designed the experiments. M.P.-D. performed the statistical analysis. O.A., W.A.-J., and M.G. performed literature mining. P.H., D.T., F.B., L.S., J.C., C.L.-L., and V.S. participated in and supervised the statistical analysis. M.G. and V.S. wrote the manuscript. V.S. supervised the study.

DECLARATION OF INTERESTS

The authors declare no competing interests.

Received: February 19, 2019
Revised: June 20, 2019
Accepted: September 9, 2019
Published: October 3, 2019

REFERENCES

Abou-Jaoudé, W., Monteiro, P.T., Naldi, A., Grandclaudon, M., Soumelis, V., Chaouiya, C., and Thieffry, D. (2015). Model checking to assess T-helper cell plasticity. Front. Bioeng. Biotechnol. *2*, 86.

Acosta-Rodriguez, E.V., Napolitani, G., Lanzavecchia, A., and Sallusto, F. (2007). Interleukins 1beta and 6 but not transforming growth factor-beta are essential for the differentiation of interleukin 17-producing human T helper cells. Nat. Immunol. *8*, 942–949.

Alculumbre, S., and Pattarini, L. (2016). Purification of Human Dendritic Cell Subsets from Peripheral Blood. Methods Mol. Biol. *1423*, 153–167.

Antebi, Y.E., Reich-Zeliger, S., Hart, Y., Mayo, A., Eizenberg, I., Rimer, J., Putheti, P., Pe'er, D., and Friedman, N. (2013). Mapping differentiation under mixed culture conditions reveals a tunable continuum of T cell fates. PLoS Biol. *11*, e1001616.

Balan, S., Arnold-Schrauf, C., Abbas, A., Couespel, N., Savoret, J., Imperatore, F., Villani, A.C., Vu Manh, T.P., Bhardwaj, N., and Dalod, M. (2018). Large-Scale Human Dendritic Cell Differentiation Revealing Notch-Dependent Lineage Bifurcation and Heterogeneity. Cell Rep. *24*, 1902–1915.e6.

Banchereau, J., and Steinman, R.M. (1998). Dendritic cells and the control of immunity. Nature *392*, 245–252.

Cariani, F., and Rips, L.J. (2017). Conditionals, Context, and the Suppression Effect. Cogn. Sci. (Hauppauge) *41*, 540–589.

Chen, L., and Flies, D.B. (2013). Molecular mechanisms of T cell co-stimulation and co-inhibition. Nat. Rev. Immunol. *13*, 227–242.

Ciofani, M., Madar, A., Galan, C., Sellars, M., Mace, K., Pauli, F., Agarwal, A., Huang, W., Parkhurst, C.N., Muratet, M., et al. (2012). A validated regulatory network for Th17 cell specification. Cell *151*, 289–303.

da Silva-Diz, V., Lorenzo-Sanz, L., Bernat-Peguera, A., Lopez-Cerda, M., and Muñoz, P. (2018). Cancer cell plasticity: Impact on tumor progression and therapy response. Semin. Cancer Biol. *53*, 48–58.

Edfors, F., Danielsson, F., Hallström, B.M., Käll, L., Lundberg, E., Pontén, F., Forsström, B., and Uhlén, M. (2016). Gene-specific correlation of RNA and protein levels in human cells and tissues. Mol. Syst. Biol. *12*, 883.

Guermonprez, P., Valladeau, J., Zitvogel, L., Théry, C., and Amigorena, S. (2002). Antigen presentation and T cell stimulation by dendritic cells. Annu. Rev. Immunol. *20*, 621–667.

Ito, T., Wang, Y.H., Duramad, O., Hori, T., Delespesse, G.J., Watanabe, N., Qin, F.X., Yao, Z., Cao, W., and Liu, Y.J. (2005). TSLP-activated dendritic cells induce an inflammatory T helper type 2 cell response through OX40 ligand. J. Exp. Med. *202*, 1213–1223.

Ivanov, I.I., McKenzie, B.S., Zhou, L., Tadokoro, C.E., Lepelley, A., Lafaille, J.J., Cua, D.J., and Littman, D.R. (2006). The orphan nuclear receptor RORgammat directs the differentiation program of proinflammatory IL-17+ T helper cells. Cell *126*, 1121–1133.

Keller, R. (2001). Dendritic cells: their significance in health and disease. Immunol. Lett. *78*, 113–122.

Kintsch, W., and Mangalath, P. (2011). The construction of meaning. Top. Cogn. Sci. *3*, 346–370.

Korn, T., Bettelli, E., Oukka, M., and Kuchroo, V.K. (2009). IL-17 and Th17 Cells. Annu. Rev. Immunol. *27*, 485–517.

Liu, Y.J., Kanzler, H., Soumelis, V., and Gilliet, M. (2001). Dendritic cell lineage, plasticity and cross-regulation. Nat. Immunol. *2*, 585–589.

Liu, Y., Beyer, A., and Aebersold, R. (2016). On the Dependency of Cellular Protein Levels on mRNA Abundance. Cell *165*, 535–550.

Macagno, A., Napolitani, G., Lanzavecchia, A., and Sallusto, F. (2007). Duration, combination and timing: the signal integration model of dendritic cell activation. Trends Immunol. *28*, 227–233.

Manel, N., Unutmaz, D., and Littman, D.R. (2008). The differentiation of human T(H)-17 cells requires transforming growth factor-beta and induction of the nuclear receptor RORgammat. Nat. Immunol. *9*, 641–649.

Meinshausen, N., and Bühlmann, P. (2010). Stability selection. J. R. Stat. Soc. Series B. Stat. Methodol. *72*, 417–473.

Nakayama, T., Hirahara, K., Onodera, A., Endo, Y., Hosokawa, H., Shinoda, K., Tumes, D.J., and Okamoto, Y. (2017). Th2 Cells in Health and Disease. Annu. Rev. Immunol. *35*, 53–84.

Naldi, A., Carneiro, J., Chaouiya, C., and Thieffry, D. (2010). Diversity and plasticity of Th cell types predicted from regulatory network modelling. PLoS Comput. Biol. *6*, e1000912.

Perrot-Dockès, M., Lévy-Leduc, C., Chiquet, J., Sansonnet, L., Brégère, M., Étienne, M.P., Robin, S., and Genta-Jouve, G. (2018a). A variable selection approach in the multivariate linear model: an application to LC-MS metabolomics data. Stat. Appl. Genet. Mol. Biol. *17*, /j/sagmb.2018.17.issue-5/sagmb-2017-0077/sagmb-2017-0077.xml.

Perrot-Dockès, M., Lévy-Leduc, C., Sansonnet, L., and Chiquet, J. (2018b). Variable selection in multivariate linear models with high-dimensional covariance matrix estimation. J. Multivariate Anal. *166*, 78–97.

Soumelis, V., Reche, P.A., Kanzler, H., Yuan, W., Edward, G., Homey, B., Gilliet, M., Ho, S., Antonenko, S., Lauerma, A., et al. (2002). Human epithelial cells trigger dendritic cell mediated allergic inflammation by producing TSLP. Nat. Immunol. *3*, 673–680.

Tibshirani, R. (1996). Regression Shrinkage and Selection via the Lasso. J. R. Stat. Soc. Series B Stat. Methodol. *58*, 267–288.

Tindemans, I., Peeters, M.J.W., and Hendriks, R.W. (2017). Notch Signaling in T Helper Cell Subsets: Instructor or Unbiased Amplifier? Front. Immunol. *8*, 419.

Touzot, M., Grandclaudon, M., Cappuccio, A., Satoh, T., Martinez-Cingolani, C., Servant, N., Manel, N., and Soumelis, V. (2014). Combinatorial flexibility of cytokine function during human T helper cell differentiation. Nat. Commun. *5*, 3987.

Vento-Tormo, R., Efremova, M., Botting, R.A., Turco, M.Y., Vento-Tormo, M., Meyer, K.B., Park, J.E., Stephenson, E., Polański, K., Goncalves, A., et al. (2018). Single-cell reconstruction of the early maternal-fetal interface in humans. Nature *563*, 347–353.

Volpe, E., Servant, N., Zollinger, R., Bogiatzi, S.I., Hupé, P., Barillot, E., and Soumelis, V. (2008). A critical function for transforming growth factor-beta, interleukin 23 and proinflammatory cytokines in driving and modulating human T(H)-17 responses. Nat. Immunol. *9*, 650–657.

Wang, Y., Chen, X., Cao, W., and Shi, Y. (2014). Plasticity of mesenchymal stem cells in immunomodulation: pathological and therapeutic implications. Nat. Immunol. *15*, 1009–1016.

Yosef, N., Shalek, A.K., Gaublomme, J.T., Jin, H., Lee, Y., Awasthi, A., Wu, C., Karwacz, K., Xiao, S., Jorgolli, M., et al. (2013). Dynamic regulatory network controlling TH17 cell differentiation. Nature *496*, 461–468.

Zhu, J., Yamane, H., and Paul, W.E. (2010). Differentiation of effector CD4 T cell populations (*). Annu. Rev. Immunol. *28*, 445–489.

Zygmunt, B., and Veldhoen, M. (2011). T helper cell differentiation more than just cytokines. Adv. Immunol. *109*, 159–196.

STAR★METHODS

KEY RESOURCES TABLE

REAGENT or RESOURCE	SOURCE	IDENTIFIER
Antibodies		
FITC Mouse anti-human CD3 (Clone HIT3a)	BD	Cat# 555339; RRID:AB_395745
FITC Mouse anti-human CD14 (Clone TÜK4)	Miltenyi Biotec	Cat# 130-080-701; RRID:AB_244303
FITC Mouse anti-human CD16 (Clone NKP15)	BD	Cat# 335035
FITC Mouse anti-human CD19 (Clone LT19)	Miltenyi Biotec	Cat# 130-091-328; RRID:AB_244222
APC-Cy7 Mouse anti-human CD11c (Clone Bu15)	BioLegend	Cat# 337218; RRID:AB_10662746
PE-Cy5 Mouse anti-human CD4 (Clone 13B8.2)	Beckman Coulter	Cat# A07752
R-PE Mouse anti-human OX40L (Clone ANC10G1)	Ancell	Cat# 400-050
R-PE Mouse IgG1, κ Isotype Control (Clone MOPC31C)	Ancell	Cat# 278-050
BV711 Mouse anti-human CD54 (Clone HA58)	BD	Cat# 564078; RRID:AB_2738579
BV711 Mouse IgG1, κ Isotype Control (Clone X40)	BD	Cat# 563044
BV786 Mouse anti-human CD273 (Clone MIH18)	BD	Cat# 563843; RRID:AB_2738446
BV786 Mouse anti-human CD80 (Clone L307.4)	BD	Cat# 564159; RRID:AB_2738631
BV786 Mouse IgG1, κ Isotype Control (Clone X40)	BD	Cat# 563330
FITC Mouse anti-human CD70 (Clone Ki-24)	BD	Cat# 555834; RRID:AB_396157
FITC Mouse IgG3, κ Isotype Control (Clone J606)	BD	Cat# 555578; RRID:AB_395956
Alexa Fluor® 700 Mouse anti-human CD29 (Clone TS2/16)	BioLegend	Cat# 303020; RRID:AB_2130078
Alexa Fluor® 700 Mouse IgG1, κ Isotype Control (Clone MOPC-21)	BioLegend	Cat# 400144
APC Mouse anti-human ICAM-3 (Clone CBR-IC3/1)	BioLegend	Cat# 330011; RRID:AB_1227570
APC Mouse anti-human Jagged-2 (Clone MHJ2-523)	BioLegend	Cat# 346906 (Discontinued)
APC Mouse IgG1, κ Isotype Control (Clone MOPC-21)	BioLegend	Cat# 400121; RRID:AB_326443
BV650 Mouse anti-human CD86 (Clone IT2.2)	BioLegend	Cat# 305428; RRID:AB_2563823
BV650 Mouse IgG2b, κ Isotype Control (Clone MPC-11)	BioLegend	Cat# 400352
BV711 Mouse anti-human HLA-DR (Clone L243)	BioLegend	Cat# 307644; RRID:AB_2562913
BV711 Mouse IgG2a, κ Isotype Control (Clone MOPC-173)	BioLegend	Cat# 400272
FITC Mouse anti-human CD100 (Clone A8)	BioLegend	Cat# 328406; RRID:AB_2254362
FITC Mouse IgG1, κ Isotype Control (Clone MOPC-21)	BioLegend	Cat# 400108
FITC Mouse anti-human ICAM-2 (Clone CBR-IC2/2)	BioLegend	Cat# 328507
FITC Mouse IgG2a, κ Isotype Control (Clone MOPC-173)	BioLegend	Cat# 400209; RRID:AB_1134236
PE Mouse anti-human CD18 (Clone TS1/18)	BioLegend	Cat# 302107; RRID:AB_314225
PE Mouse anti-human Nectin-2 (Clone TX31)	BioLegend	Cat# 337410; RRID:AB_2269088
PE Mouse anti-human PVR (Clone SKII.4)	BioLegend	Cat# 337610; RRID:AB_2174019
PE Mouse IgG1, κ Isotype Control (Clone MOPC-21)	BioLegend	Cat# 400112
PE/Cy7 Mouse anti-human CD40 (Clone 5C3)	BioLegend	Cat# 334321; RRID:AB_10643414
PE/Cy7 Mouse IgG1, κ Isotype Control (Clone MOPC-21)	BioLegend	Cat# 400126; RRID:AB_326448
PE/Cy5 Mouse anti-human CD58 (Clone TS2/9)	BioLegend	Cat# 330909; RRID:AB_1227576
PE/Cy5 Mouse IgG1, κ Isotype Control (Clone MOPC-21)	BioLegend	Cat# 400117
PerCP/Cy5.5 Mouse anti-human CD83 (Clone HB15e)	BioLegend	Cat# 305320; RRID:AB_2076530
PerCP/Cy5.5 Mouse IgG1, κ Isotype Control (Clone MOPC-21)	BioLegend	Cat# 400150
Alexa Fluor® 488 Goat anti-human Galectin-3	R&D Systems	Cat# IC1154G; RRID:AB_10890949
Alexa Fluor® 488 Normal Goat IgG	R&D Systems	Cat# IC108G; RRID:AB_10890944
Alexa Fluor® 700 Mouse anti-human VISTA (Clone 730804)	R&D Systems	Cat# FAB71261N
Alexa Fluor® 700 Mouse IgG_{2B} Isotype Control (Clone 133303)	R&D Systems	Cat# IC0041N; RRID:AB_10973174
APC Mouse anti-human SLAMF3 (Clone 249936)	R&D Systems	Cat# FAB1898A; RRID:AB_2137949

(*Continued on next page*)

Continued

REAGENT or RESOURCE	SOURCE	IDENTIFIER
APC Mouse IgG_{2A} Isotype Control (Clone 20102)	R&D Systems	Cat# IC003A; RRID:AB_357243
APC Mouse anti-human 4-1BBL (Clone 282220)	R&D Systems	Cat# FAB2295A; RRID:AB_2207514
APC Mouse anti-human ICOSL (Clone 136726)	R&D Systems	Cat# FAB165A; RRID:AB_991955
APC Mouse IgG_{2B} Isotype Control (Clone 133303)	R&D Systems	Cat# IC0041A; RRID:AB_357246
FITC Mouse anti-human B7H3 (Clone 185504)	R&D Systems	Cat# FAB1027F; RRID:AB_1208024
FITC Mouse IgG_1 Isotype Control (Clone 11711)	R&D Systems	Cat# IC002F
FITC Goat anti-human SLAMF5	R&D Systems	Cat# FAB1855F (Discontinued); RRID:AB_2074764
FITC Normal Goat IgG	R&D Systems	Cat# IC108F; RRID:AB_10177332
PE Mouse anti-human LIGHT (Clone 115520)	R&D Systems	Cat# FAB664P; RRID:AB_2240851
PE Mouse IgG_1 Isotype Control (Clone 133303)	R&D Systems	Cat# IC002P; RRID:AB_357242
PE Mouse anti-human CD30L (Clone 116614)	R&D Systems	Cat# FAB1028P; RRID:AB_2207494
PE Mouse IgG2B Isotype Control (Clone 133303)	R&D Systems	Cat# IC0041P; RRID:AB_357249
PerCP Mouse anti-human CD11a (Clone CR38)	R&D Systems	Cat# FAB35951C (Discontinued); RRID:AB_10892335
PerCP Mouse IgG_{2A} Isotype Control (Clone 20102)	R&D Systems	Cat# IC003C; RRID:AB_1207937
PerCP-eFluor710 Mouse anti-human PDL1 (Clone MIH1)	ThermoFisher Scientific	Cat# 46-5983-42; RRID:AB_11041815
PerCP-eFluor710 Mouse IgG1, κ Isotype Control (Clone P3.6.2.8.1)	ThermoFisher Scientific	Cat# 46-4714-82; RRID:AB_1834453
Alexa Fluor® 488 Mouse anti-human IL-17A (Clone BL168)	BioLegend	Cat# 512308; RRID:AB_961386
Alexa Fluor® 488 Mouse IgG1, κ Isotype Control (Clone MOPC-21)	BioLegend	Cat# 400134
PE-Cy7 Rat anti-human IL-17F (Clone SHLR17)	ThermoFisher Scientific	Cat# 25-7169-42; RRID:AB_10853673
PE-Cy7 Rat IgG1, κ Isotype Control (Clone eBRG1)	ThermoFisher Scientific	Cat# 25-4301-82; RRID:AB_470198
PE Mouse anti-human IL-21 (Clone 3A3-N2)	BioLegend	Cat# 513004; RRID:AB_2249025
PE Mouse IgG1, κ Isotype Control (Clone MOPC-21)	BioLegend	Cat# 400112
eFluor 660 Mouse anti-human IL-22 (Clone 22URTI)	ThermoFisher Scientific	Cat# 50-7229-42; RRID:AB_10598650
eFluor 660 Mouse IgG1, κ Isotype Control (Clone P3.6.2.8.1)	ThermoFisher Scientific	Cat# 50-4714-82; RRID:AB_10597301
BV605 Mouse anti-human IFN-γ (Clone B27)	BD	Cat# 562974; RRID:AB_2737926
BV605 Mouse IgG1, κ Isotype Control (Clone X40)	BD	Cat# 562652; RRID:AB_2714005
Ultra-LEAF Purified anti-human CD3 Antibody (Clone OKT3)	Biolegend	Cat# 317347; RRID:AB_2571994
Ultra-LEAF Purified anti-human CD28 Antibody (Clone CD28.2)	Biolegend	Cat# 302943; RRID:AB_2616667
Mouse IgG1 kappa Isotype Control (Clone P3.6.2.8.1)	ThermoFisher Scientific	Cat# 14-4714-85; RRID:AB_470112
Human IL12 monoclonal blocking antibody (Clone B-T21)	ThermoFisher Scientific	Cat# BMS152; RRID:AB_10596494
Mouse IgG1 isotype control	R&D Systems	Cat# MAB002; RRID:AB_357344
Human CD2 monoclonal blocking antibody (Clone 299808)	R&D Systems	Cat# MAB18562
Mouse IgG2A isotype control	R&D Systems	Cat# MAB003; RRID:AB_357345
Anti-human CD28 monoclonal blocking antibody (Clone 9.3)	BioXcell	Cat# BE0248; RRID:AB_2687729
Anti-Unknown Specificity (Isotype control) Human IgG1,k	Absolute Antibody	Cat# Ab00178-10.0
Anti-human ICOS monoclonal blocking antibody	N/A	The agonist ICOS antibody was produced for research purposes from the sequence made publicly available by JOUNCE THERAPEUTICS in the patent US 2016/0304610, INC. The produced antibody corresponded to clone 37A10S713 with a human IgG1 isotype.
Biological Samples		
Human Healthy blood donors for primary MoDC, bDC, naive and memory CD4 T cells	Etablissement Français du Sang (French Blood Bank)	N/A
Human serum	Sigma-Aldrich	Cat# H4522

(*Continued on next page*)

Continued

REAGENT or RESOURCE	SOURCE	IDENTIFIER
Chemicals, Peptides and Recombinant Proteins		
Lymphoprep	StemCell Technologies	Cat# 07861
RPMI 1640 Medium, GlutaMAX Supplement	ThermoFisher Scientific	Cat# 61870010
Penicillin-Streptomycin	ThermoFisher Scientific	Cat# 15140122
Foetal Bovine Serum Research Grade	Hyclone/Perbio	Cat# CH30160.03
MEM Non-essential Amino Acids Solution (100X)	ThermoFisher Scientific	Cat# 11140050
Sodium pyruvate (100 mM)	ThermoFisher Scientific	Cat#11360070
X-VIVO 15 Chemically Defined, Serum-Free Hematopoietic Cell Medium	Ozyme	Cat# BE02-060F
HEPES Buffer	ThermoFisher Scientific	Cat# 15630056
UltraPure EDTA	ThermoFisher Scientific	Cat# 15575020
Phorbol 12-myristate 13-acetate	Sigma-Aldrich	Cat# P8139
Ionomycin calcium salt from Streptomyces conglobatus	Sigma-Aldrich	Cat# I0634
Brefeldin A Solution 1000X	ThermoFisher Scientific	Cat# 00-4506-51
Intracellular Fixation & Permeabilization Buffer Set	ThermoFisher Scientific	Cat# 88-8824-00
DAPI (4',6-Diamidino-2-Phenylindole, Dihydrochloride)	ThermoFisher Scientific	Cat# D1306
Zombie NIR Fixable Viability Kit	BioLegend	Cat# 423105
LIVE/DEAD Fixable Yellow Dead Cell Stain Kit	ThermoFisher Scientific	Cat# L34959
CellTrace Violet Cell Proliferation Kit, for flow cytometry	ThermoFisher Scientific	Cat# C34557
Recombinant human IL-1α	R&D Systems	Cat# 200-LA
Recombinant human IL-1β	Peprotech	Cat# 200-01B
Recombinant human IL-4	R&D Systems	Cat# 204-IL-010
Recombinant human IL-6	Peprotech	Cat# 200-06
Recombinant human IL-12p70	R&D Systems	Cat# 219-IL
Recombinant human IL-23	R&D Systems	Cat# 1290-IL
Recombinant human TGF-β1	Peprotech	Cat# 100-21
Recombinant human IL-4	Miltenyi Biotec	Cat# 130-093-922
Recombinant human GM-CSF	Miltenyi Biotec	Cat# 130-093-865
PAM3CSK4	Invivogen	Cat# tlrl-pms
Aluminum potassium sulfate	Invivogen	Cat# tlrl-alk
Heat-killed Staphylococcus aureus	Invivogen	Cat# tlrl-hksa
Heat-killed Candida albicans	Invivogen	Cat# tlrl-hkca
Heat-killed Listeria monocytogenes	Invivogen	Cat# tlrl-hklm
Heat-killed Streptococcus pneumoniae	Invivogen	Cat# tlrl-hksp
Poly(I:C) High molecular weight	Invivogen	Tlrl-pic
Curdlan	Invivogen	Cat# tlrl-curd
Zymosan	Sigma-Aldrich	Cat# Z4250
LPS-EB Ultrapure	Invivogen	Cat# tlrl-3pelps
Prostaglandin E2	Sigma-Aldrich	Cat# P0409
R848	Invivogen	Cat# tlrl-r848
Recombinant Human IFN-β	Preprotech	Cat# 300-02BC
Influenza A/PR/8/34 (H1N1) Allantoic Fluid	Charles River	Cat# 10100781
Recombinant human TSLP	R&D Systems	Cat# 1398-TS
Critical Commercial Assays		
EasySep Human Pan-DC Pre-Enrichment Kit	StemCell Technologies	Cat# 19251
EasySep Human Naive CD4+ T Cell Isolation Kit	StemCell Technologies	Cat# 19555
CD14 MicroBead human	Miltenyi Biotec	Cat# 130-050-201
LS columns	Miltenyi Biotec	Cat# 130-042-401

(*Continued on next page*)

Continued

REAGENT or RESOURCE	SOURCE	IDENTIFIER
Memory CD4+ T Cell Isolation Kit, human	Miltenyi Biotec	Cat# 130-091-893
Dynabeads® Human T-Activator CD3/CD28 for T Cell Expansion and Activation	ThermoFisher Scientific	Cat# 11131D
Easy 50 EasySep Magnet	StemCell Technologies	Cat# 18002
Big Easy EasySep Magnet	StemCell Technologies	Cat# 18001
QuadroMACS Starting Kit (LS)	Miltenyi Biotec	Cat# 130-091-051
BD Cytometric Bead Array (CBA) Human Soluble Protein Master Buffer Kit	BD	Cat# 558265
BD Cytometric Bead Array (CBA) Human IL-1α Flex Set	BD	Cat# 560153
BD Cytometric Bead Array (CBA) Human IL-1β Flex Set	BD	Cat# 558279
BD Cytometric Bead Array (CBA) Human IL-2 Flex Set	BD	Cat# 558270
BD Cytometric Bead Array (CBA) Human IL-3 Flex Set	BD	Cat# 558355
BD Cytometric Bead Array (CBA) Human IL-4 Flex Set	BD	Cat# 558272
BD Cytometric Bead Array (CBA) Human IL-5 Flex Set	BD	Cat# 558278
BD Cytometric Bead Array (CBA) Human IL-6 Flex Set	BD	Cat# 558276
BD Cytometric Bead Array (CBA) Human IL-9 Flex Set	BD	Cat# 558333
BD Cytometric Bead Array (CBA) Human IL-10 Flex Set	BD	Cat# 558274
BD Cytometric Bead Array (CBA) Human IL-12p70 Flex Set	BD	Cat# 558283
BD Cytometric Bead Array (CBA) Human IL-13 Flex Set	BD	Cat# 558450
BD Cytometric Bead Array (CBA) Human IL-17A Flex Set	BD	Cat# 560383
BD Cytometric Bead Array (CBA) Human IL-17F Flex Set	BD	Cat# 562151
BD Cytometric Bead Array (CBA) Human GM-CSF Flex Set	BD	Cat# 558335
BD Cytometric Bead Array (CBA) Human IFN-γ Flex Set	BD	Cat# 558269
BD Cytometric Bead Array (CBA) Human TNF-α Flex Set	BD	Cat# 558273
MILLIPLEX MAP Human TH17 Magnetic Bead Panel - Immunology Multiplex Assay IL-21, IL-22, IL-31, TNF-β	Merck Millipore	Cat# HTH17MAG-14K
MILLIPLEX MAP Human TH17 Magnetic Bead Panel - Immunology Multiplex Assay IL-23, IL-28α	Merck Millipore	Cat# HTH17MAG-14K
RNeasy Micro Kit (50)	QIAGEN	Cat# 74004
SuperScript II Reverse Transcriptase	ThermoFisher Scientific	Cat# 18064-071
Random primers	Promega	Cat# C1181
Oligo(dT)15 Primer	Promega	Cat# C1101
RNasin® Ribonuclease Inhibitors	Promega	Cat# N2515
dNTP	Promega	Cat# U1240
qPCR MasterMix Plus dTTP	Eurogentec	Cat# 05-QP2X-03+WOUN
Oligonucleotides		
RORC [Hs01076112_m1]	ThermoFisher Scientific	Cat# 4331182
TBX21 [Hs00203436_m1]	ThermoFisher Scientific	Cat# 4331182
GATA3 [Hs00231122_m1]	ThermoFisher Scientific	Cat# 4331182
RORA [Hs00536545_m1]	ThermoFisher Scientific	Cat# 4331182
FOXP3 [Hs00203958_m1]	ThermoFisher Scientific	Cat# 4331182
FOXP1 [Hs00212860_m1]	ThermoFisher Scientific	Cat# 4331182
SH2D1A [Hs00158978_m1]	ThermoFisher Scientific	Cat# 4331182
PRDM1 [Hs00153357_m1]	ThermoFisher Scientific	Cat# 4331182
PDCD1 [Hs01550088_m1]	ThermoFisher Scientific	Cat# 4331182
BTLA [Hs00699198_m1]	ThermoFisher Scientific	Cat# 4331182
HLX [Hs00172035_m1]	ThermoFisher Scientific	Cat# 4331182
IRF1 [Hs00971965_m1]	ThermoFisher Scientific	Cat# 4331182

(*Continued on next page*)

Continued

REAGENT or RESOURCE	SOURCE	IDENTIFIER
CMIP [Hs00286832_m1]	ThermoFisher Scientific	Cat# 4331182
MAF [Hs00193519_m1]	ThermoFisher Scientific	Cat# 4331182
RUNX1 [Hs00231079_m1]	ThermoFisher Scientific	Cat# 4331182
PU1 / SPI1 [Hs02786711_m1]	ThermoFisher Scientific	Cat# 4331182
CD200 [Hs01033303_m1]	ThermoFisher Scientific	Cat# 4331182
CXCL13 [Hs00757930_m1]	ThermoFisher Scientific	Cat# 4331182
IL-12RB2 [Hs00155486_m1]	ThermoFisher Scientific	Cat# 4331182
BCL6 [Hs00153368_m1]	ThermoFisher Scientific	Cat# 4331182
IRF4 [Hs00180031_m1]	ThermoFisher Scientific	Cat# 4331182
FOSL2 [Hs01050117_m1]	ThermoFisher Scientific	Cat# 4331182
BATF [Hs00232390_m1]	ThermoFisher Scientific	Cat# 4331182
KDM6B [Hs00996325_g1]	ThermoFisher Scientific	Cat# 4331182
NFKBIZ [Hs00230071_m1]	ThermoFisher Scientific	Cat# 4331182
SATB1 [Hs00962580_m1]	ThermoFisher Scientific	Cat# 4331182
BCL11B [Hs01102259_m1]	ThermoFisher Scientific	Cat# 4331182
EOMES [Hs00172872_m1]	ThermoFisher Scientific	Cat# 4331182
SKI [Hs01057032_m1]	ThermoFisher Scientific	Cat# 4331182
ATF6 [Hs00232586_m1]	ThermoFisher Scientific	Cat# 4331182
AES [Hs01081012_m1]	ThermoFisher Scientific	Cat# 4331182
CREM [Hs01582003_g1]	ThermoFisher Scientific	Cat# 4331182
DDIT3 [Hs00358796_g1]	ThermoFisher Scientific	Cat# 4331182
LEF1 [Hs01547250_m1]	ThermoFisher Scientific	Cat# 4331182
NFATC2 [Hs00905451_m1]	ThermoFisher Scientific	Cat# 4331182
ETV6 [Hs00231101_m1]	ThermoFisher Scientific	Cat# 4331182
SIRT2 [Hs01560289_m1]	ThermoFisher Scientific	Cat# 4331182
USP18 [Hs00276441_m1]	ThermoFisher Scientific	Cat# 4331182
NFATC1 [Hs00542675_m1]	ThermoFisher Scientific	Cat# 4331182
NFATC3 [Hs00190046_m1]	ThermoFisher Scientific	Cat# 4331182
SMAD3 [Hs00969210_m1]	ThermoFisher Scientific	Cat# 4331182
SMAD2 [Hs00998187_m1]	ThermoFisher Scientific	Cat# 4331182
SMAD7 [Hs00998193_m1]	ThermoFisher Scientific	Cat# 4331182
MINA [Hs01031255_m1]	ThermoFisher Scientific	Cat# 4331182
POUA2F1 [Hs01573369_m1]	ThermoFisher Scientific	Cat# 4331182
TNFRSF4/OX40 [Hs00937195_g1]	ThermoFisher Scientific	Cat# 4331182
TNFRSF8/CD30 [Hs00174277_m1]	ThermoFisher Scientific	Cat# 4331182
TIGIT [Hs00545087_m1]	ThermoFisher Scientific	Cat# 4331182
CD226/DNAM-1 [Hs00170832_m1]	ThermoFisher Scientific	Cat# 4331182
CD96 [Hs00976975_m1]	ThermoFisher Scientific	Cat# 4331182
IL17A [Hs00174383_m1]	ThermoFisher Scientific	Cat# 4331182
IL17F [Hs00369400_m1]	ThermoFisher Scientific	Cat# 4331182
STAT3 [Hs00374280_m1]	ThermoFisher Scientific	Cat# 4331182
ICOS [Hs00359999_m1]	ThermoFisher Scientific	Cat# 4331182
IL23R [Hs00332759_m1]	ThermoFisher Scientific	Cat# 4331182
AHR [Hs00169233_m1]	ThermoFisher Scientific	Cat# 4331182
IL1R2 [Hs01030384_m1]	ThermoFisher Scientific	Cat# 4331182
CCL20 [Hs01011368_m1]	ThermoFisher Scientific	Cat# 4331182
IL2RA [Hs00907779_m1]	ThermoFisher Scientific	Cat# 4331182
IL2RB [Hs01081697_m1]	ThermoFisher Scientific	Cat# 4331182

(*Continued on next page*)

Continued

REAGENT or RESOURCE	SOURCE	IDENTIFIER
IL2RG [Hs00953624_m1]	ThermoFisher Scientific	Cat# 4331182
IL17RA [Hs01064648_m1]	ThermoFisher Scientific	Cat# 4331182
CCR6 [Hs00171121_m1]	ThermoFisher Scientific	Cat# 4331182
B2M [Hs99999907_m1]	ThermoFisher Scientific	Cat# 4331182
RPL34 [Hs00241560_m1]	ThermoFisher Scientific	Cat# 4331182
Software and Algorithms		
GraphPad Prism 6 – Version 6.01	GraphPad	https://www.graphpad.com/
FlowJo V10 – Version 10.0.8	FlowJo	https://www.flowjo.com
Bioplex Manager Software	BioRad	https://www.bio-rad.com/en-cn/product/bio-plex-manager-software-standard-edition?ID=5846e84e-03a7-4599-a8ae-7ba5dd2c7684
FCAP Array – Version 3.0	BD	http://www.bdbiosciences.com/us/applications/research/bead-based-immunoassays/analysis-software/fcap-array-software-v30/p/652099
R version 3.5.2	The R Foundation	https://www.r-project.org/

LEAD CONTACT AND MATERIALS AVAILABILITY

Further information and requests for resources and reagents should be directed to and will be fulfilled by the Lead Contact, Vassili Soumelis (vassili.soumelis@curie.fr). This study did not generate new unique reagents.

EXPERIMENTAL MODEL AND SUBJECT DETAILS

Human subjects

Apheresis blood from healthy human blood donors were obtained from Etablissement Français du Sang (French Blood Establishment) after written informed consent and in conformity with Institut Curie ethical guidelines. Gender identity and age from anonymous donors were not available, but all donors were between 18 and 70 years old (age limits for blood donation in France).

METHOD DETAILS

PBMCs purification

PBMCs were isolated by centrifugation on a density gradient (Lymphoprep, Proteogenix).

MoDC generation and activation

$CD14^+$ cells were selected from PBMCs using magnetically labeled anti-CD14 Microbeads and MACS LS columns following manufacturer's instructions (MiltenyiBiotec). $CD14^+$ cells were then cultured with IL-4 (50 ng/mL) and GM-CSF (10 ng/mL) (MiltenyiBiotec) for 5 days in RPMI 1640 Medium, GlutaMAX (Life Technologies) with 10% Fetal Calf Serum. Monocyte-derived Dendritic Cells (MoDC) were activated for 24 hours using one or a combination of perturbators as described in Table S1.

Blood dendritic cells purification

A step of DC pre-enrichment was performed from PBMCs using the EasySep Human Pan-DC Pre-Enrichment kit (StemCell Technologies). Total DC were sorted on a MoFloAstrios (Beckman Coulter) as Lineage (CD3, CD14, CD16, and $CD19)^-$, $CD4^+$ (Beckman Coulter), $CD11c^+$ (BD), as described in Alculumbre and Pattarini (2016).

$CD4^+$ T lymphocytes purification

Naive $CD4^+$ T lymphocytes were purified from PBMCs using the EasySep Human Naive CD4+ T Cell Isolation Kit (StemCell Technologies). Memory $CD4^+$ T cells were purified from PBMCs using the Memory $CD4^+$ T cell isolation Kit (MiltenyiBiotec).

Paired protein measurement in DC/T coculture

After 24 hours DC or MoDC activation with DC stimuli listed in Table S1, culture supernatants were kept for cytokine analysis for IL-23, IL-28α, IL-1, IL-10, IL-12p70, IL-6, TNF-α, while cells were washed in PBS. Some cells were used for for surface staining of the

following markers: B7H3, CD30L, 4-1BBL, PDL2, VISTA, CD40, CD54, CD58, ICAM-2, ICAM-3, CD18, CD29, SLAMF5, SLAMF3, PVR, CD11a, CD100, LIGHT, Nectin-2, Jagged-2, Galectin-3, CD70, CD80, CD83, OX40L, PDL1, CD86, ICOSL and HLA-DR. And the remaining cells were put in coculture with allogeneic naive CD4 T cells, at a ratio of 1 DC for 5 T cells, in X-VIVO 15 medium (Lonza). For FACS staining, a single batch of commercially available antibodies was used across the study.After 6 days of coculture, T cells were washed and live cells were counted at the microscope using trypan blue to calculate Exp Fold. T cells were reseeded at $1x10^6$/mL and restimulated with anti-CD3/CD28 Dynabeads (LifeTechnologies). 24 hours later supernatants were collected to measure the following T cell cytokines: IL-2, IL-3, IL-4, IL-5, IL-6, IL-9, IL-10, IL-13, IL-17A, IL-17F, IL-21, IL-22, IL-31, GM-CSF, IFN-γ, TNF-α, TNF-β. In each coculture experiment, one single DC donor was coupled to a different single CD4 T cell donor. For each DC/T cell pair, the measurement of DC derived signals and Th cytokines were performed in parallel, leading to the acquisition of paired data for the 36 DC derived signals and the 18 T cell parameters measured.

IL-12 blocking experiment

For IL-12 blocking experiment, after 24 hours activation with Zymosan (10μg/mL) or curdlan (10 μg/mL), MoDC were incubated during one hour at 37°C in the presence of 20 μg/mL of anti-IL-12p70 blocking antibody or its matched isotype control. Then, naive CD4 T cells were added to the culture. Antibodies were maintained for the duration of the co-culture. After 6 days of coculture cells were washed and reseeded at $1x10^6$/mL and restimulated with anti-CD3/CD28 Dynabeads (LifeTechnologies). 24 hours later supernatants were collected to measure T cell cytokines.

CD28 blocking experiment

For CD28 blocking experiment, MoDC were first activated for 24 hours with Flu (1X), LPS (100ng/mL) or Zymosan (10 μg/mL). Then, activated DC were cocultured with allogeneic naive CD4 T cells in the presence of 5 μg/mL anti-CD28 blocking antibody or its matched isotype control (Figure 5A). Antibodies were maintained for the duration of the co-culture. After 6 days of coculture cells were washed and reseeded at $1x10^6$/mL and restimulated with anti-CD3/CD28 Dynabeads (LifeTechnologies). 24 hours later supernatants were collected to measure T cell cytokines. We systematically measured all Th outputs predicted to be associated either to CD80 or CD86 (Figure 5B). Finally, we compared the estimated (*in silico* prediction) and the real (experimental) fold change (FC) (Figure 5B). A FC higher or lower than one for a given Th output indicated an inhibitory versus inducer role of CD80/CD86, respectively.

Addition of rhIL-12p70 during DC/T coculture

Sorted myeloid-DC were activated for 24 hours with zymosan (10 μg/mL) or HKSA (MOI 1). Then, 10,000 activated DC were cocultured with 50,000 allogeneic naive CD4 T cells in the presence or absence of 10 ng/mL rhIL-12p70. After 6 days of coculture, 100,000 T cells were restimulated for 24 hours with anti-CD3/CD28 Dynabeads. Supernatants were then collected for cytokine measurements.

DC-free Th cell polarization

Naive CD4 T cells were cultured for 5 days with only anti-CD3/CD28 Dynabeads (Life Technologies) to obtain Th0 or in combination with either 10 ng/mL IL-12 (Th1), 25ng/mL IL-4 (Th2), 10 ng/mL IL-1β or IL-1α, 100 ng/mL IL-23, IL-12 plus IL-1β or a mix of IL-1β, IL-23, 1 ng/mL TGF-β and 20 ng/mL IL-6 to obtain Th17 (Peprotech) as already published (Touzot et al., 2014). At the end of the culture cells were used for intracellular staining or washed, reseeded at $1x10^6$/mL and restimulated with anti-CD3/CD28 Dynabeads (Life Technologies) for 24 hours before collecting supernatants for cytokine measure and lysing cells in RLT buffer (QIAGEN) for qPCR analysis.

ICOS agonism

For experiments with anti-ICOS antibody, prior to culture 5 μg/mL anti-CD3 (OKT3 clone, Biolegend) with 5 μg/mL anti-ICOS or matching isotype control were coated on a flat-bottom 96 well plate (TPP) and incubated overnight at 4°C. The plate was then washed 3 times with PBS before seeding 32,000 naive CD4 T cells with 1 μg/mL anti-CD28 (CD28.2 clone, Biolegend) and cytokines as described above in X-vivo medium (Lonza). After 5 days culture, T cells were counted and 100,000 cells were restimulated with anti-CD3/CD28 Dynabeads for 24 hours before collecting supernatants for cytokine measure.

We were able to induce the following Th outputs in the Th0 condition: Exp Fold, IL,3, IL-5, IL-6, IL-10, IL-13, IL-22, TNF-α and GM-CSF (Figure 5E). In a Th17 condition, we were able to demonstrate a positive effect of the ICOS pathway on the production of IL-17A (Figure 5E). All these observations were statistically significant, and validated the model predictions. However, six predictions on TNF-β, IL-2, IL-21, IL-17F, IL-4 and IL-31 could not be validated using these experimental settings (Figure S4C). For IL-17F, IL-4 and IL-31 we could not detect a significant effect of ICOS (Figure S4C), suggesting possible lack of a co-factor. However, for TNF-β, IL-2, IL-21 we found significant but opposite effects to the one predicted by the model, including the positive role of ICOSL in the induction of IL-21 (Table S3).

CD2 agonism

For experiments with anti-CD2 agonist antibody, prior to culture 5 μg/mL anti-CD3 (OKT3 clone, Biolegend) with 5 μg/mL anti-CD2 or matching isotype control were coated on a flat-bottom 96 well plate (TPP) and incubated overnight at 4°C. The plate was then washed

3 times with PBS before seeding 32,000 naive CD4 T cells with 1 μg/mL anti-CD28 (CD28.2 clone, Biolegend) and cytokines as described above in X-vivo medium (Lonza). After 5 days culture, T cells were counted and 100,000 cells were restimulated with anti-CD3/CD28 Dynabeads for 24 hours before collecting supernatants for cytokine measure.

We showed that our anti-CD2 antibody worked by studying the Exp Fold of naive T cells, cultured with anti-CD3 and CD28 with or without anti-CD2. We found that anti-CD2 significantly induced T cell Exp Fold (Figure S7G).

Flow cytometry analysis

Antibodies and matched isotypes were titrated on the relevant human PBMC population. For surface FACS analysis on activated MoDC and blood DC the complete list of antibodies and important information such as brand, final dilutions, reference, clone and colors are given in Key Resources Table. Dead cells were excluded using DAPI (Miltenyi Biotec).

For intracellular cytokine staining, naive or memory CD4 T cells were stimulated with 100 ng/mL PMA, 500 ng/mL ionomycin and 3 μg/mL Brefeldin A (ThermoFisher) for 5 hours. To exclude dead cells, CD4 T cells were stained using the LIVE/DEAD Fixable yellow dead cell stain kit, following manufacturer's instructions (LifeTechnologies). Cells were fixed and permeabilized using the IC Fix and Permeabilization buffers (ThermoFisher). Intracellular cytokines were revealed with fluorescently conjugated antibodies against IL-17A (BioLegend), IL-17F (ThermoFisher), IL-21 (BioLegend), IL-22 (ThermoFisher), and IFN-γ (BD), or matched isotype controls and acquired on a Fortessa instrument (BD).

Cytokine quantification

Cytokines were quantified in dendritic cell supernatants using CBA flex set for IL-1α, IL-1β, IL-6, IL-10, TNF-α and IL-12p70 (also named IL-12) and using Luminex for IL-23 and IL-28α. Cytokines from T cell supernatants were quantified using CBA flex set for, IL-2, IL-3, IL-4, IL-5, IL-6, IL-9, IL-10, IL-13, IL-17A, IL-17F, TNF-α, IFN-γ and GM-CSF (BD) and Luminex for IL-21, IL-22, IL-31 and TNF-β following the manufacturer's protocol.

Gene expression quantification

At the end of the 5 days Th polarization and 24 hours restimulation, total RNA was extracted from 100,000 cells using RNA easy micro kit (QIAGEN). Total RNA was retrotranscribed using Superscript II Reverse Transcriptase (ThermoFisher Scientific) in combination with random primers, Oligo(dT) and dNTP (Promega). Transcripts were then quantified by real time PCR on a 480 LightCycler Instrument (Roche). Reactions were performed using a qPCR Master Mix Plus (Eurogentec) and TaqMan assays listed in the Key Resources Table. Raw expression data (ct values) were normalized on the mean of two housekeeping genes (B2M and RPL34).

Anti-human ICOS monoclonal blocking antibody

The agonist ICOS antibody was produced for research purposes from the sequence made publicly available by JOUNCE THERAPEUTICS in the patent US 2016/0304610, INC. The produced antibody corresponded to the following sequences of the clone 37A10S713 with a human IgG1 isotype.

Heavy chain: EVQLVESGGGLVQPGGSLRLSCAASGFTFSDYWMDWVRQAPGKGLVWVSNIDEDGSITEYSPFVKGRFTISRDNAKN TLYLQMNSLRAEDTAVYYCTRWGRFGFDSWGQGTLVTVSSASTKGPSVFPLAPSSKSTSGGTAALGCLVKDYFPEPVTVSWNSGALTS GVHTFPAVLQSSGLYSLSSVVTVPSSSLGTQTYICNVNHKPSNTKVDKKVEPKSCDKTHTCPPCPAPELLGGPSVFLFPPKPKDTLMISR TPEVTCVVVDVSHEDPEVKFNWYVDGVEVHNAKTKPREEQYNSTYRVVSVLTVLHQDWLNGKEYKCKVSNKALPAPIEKTISKAKGQPR EPQVYTLPPSREEMTKNQVSLTCLVKGFYPSDIAVEWESNGQPENNYKTTPPVLDSDGSFFLYSKLTVDKSRWQQGNVFSCSVMHEAL HNHYTQKSLSLSPGK

Light chain: IVMTQSPDSLAVSLGERATINCKSSQSLLSGSFNYLTWYQQKPGQPPKLLIFYASTRHTGVPDRFSGSGSGTDFTLTISS LQAEDVAVYYCHHHYNAPPTFGPGTKVDIKRTVAAPSVFIFPPSDEQLKSGTASVVCLLNNFYPREAKVQWKVDNALQSGNSQESVTEQ DSKDSTYSLSSTLTLSKADYEKHKVYACEVTHQGLSSPVTKSFNRGEC

Classical quality controls were performed to check that the produced anti-ICOS antibody had a correct, Purity (SDS-PAGE reducing), Homogeneity (SEC-MALS) Mass (LC-MS) and binding to target (FACS).

QUANTIFICATION AND STATISTICAL ANALYSIS

Dataset quality control – batch effect

As quality control of our procedure we asked whether experimental batch effect could play a role in the differences we observed across our dataset. Selecting the 6 most frequent perturbators within our MoDC dataset we performed principal component analysis to look for batch effects related to the date of the experiments or the donor variability (Figure S1C).

Dataset quality control – T cell expansion

As a control, we could see that the Exp Fold profiles of CD4 T cells matched the activation profiles of DC observed in Figure 1C. Indeed, T cells co-cultured with either LPS-MoDC, Zymosan-MoDC or Flu-DC induced significantly more expansion than the negative Medium-DC control reflecting good quality controls of the experiments (Figure 3B).

Statistical tests

In the figure legends, n is indicated and corresponds to the number of donors used for each experiment. Paired Wilcoxon or t test were applied as detailed in figure legends to compare two groups. Significance was retained for *, $p < 0.05$.

Statistical analysis

Each variable of the dataset was transformed using first the Box-Cox transformation and then a scaling step on both the mean and the variance (using TBoCo package). For all analyses performed, cytokine values inferior to 20 pg/mL were considered as 0, as 20 pg/mL corresponds to the general detection limit of the assay. In order to cluster the inputs, outputs and the samples a hierarchical clustering approach was applied by using different criterions: Ward's criterion and Pearson correlation metric were used to cluster the inputs and the outputs, while Ward's criterion and the Euclidean metric were used to cluster the samples or DC conditions. The heatmaps were generated by using the heatmap.2 package. The correlations between the continuous variables were computed by using the Pearson correlation. All statistical tests are called ''significant'' if their p value is smaller than 0.05. The p values were corrected using Benjamini-Hochberg correction.

Boxplots represented are Tukey Boxplot, meaning that the box goes from the first to the third quartile, it is cut by the median and the whisker goes from the upper (resp. the lower) whisker extends from the third (resp. the first) quartile to the largest (resp. the smallest) value no further than 1.5 * IQR from the third (resp. The first) quartile (where IQR is the inter-quartile range, or distance between the first and third quartiles). Data beyond the end of the whiskers points and are plotted individually.

The fold change represented in Figures 5B and S4A represent the value (real or estimated) of an output in the absence of CD80 and CD86 divided by the value of the output in the same sample when CD80 and CD86 are present.

Model comparison and ROC Curves

In order to test different multivariate statistical modeling strategies, and to compare them in terms of false and true positive rates, we generated a simulated dataset that mimics the features of our DC and T cell experimental data, but for which we arbitrarily attributed a link between DC communication signals and Th cytokines, the whole strategy is detailed below.

The Figure S3A aims at assessing the performance of our modeling strategy in terms of variable selection and comparing it with other variable selection methodologies. In order to do this, we performed numerical experiment: we used the real input dataset called hereafter X, simulated a random error matrix (E) with a block covariance matrix to mimic the Th subset and a matrix of coefficients (B) to mimic the effect of the inputs on the outputs. Using these three matrices we created a new output matrix $Y = XB+E$. On this new matrix Y we applied different modeling strategies. 1) The sPLS, 2) the classical Lasso, applied to each column of Y (namely each output) independently (Lasso without covariance) 3) Our methodology, called MultivarSel, (described in the Modeling strategy section), which consists in estimating the covariance matrix of E and use it to remove the dependence between the outputs before applying the Lasso methodology (Lasso empirical covariance) 4) Lasso with real covariance matrix, the same methodology than ours, but with the real covariance matrix of E, corresponding to the internal positive control of this analysis. We also assessed stability selection by adding this analysis step to the three last methods (Lasso with stability selection and without covariance, Lasso with stability selection and empirical covariance, Lasso with stability selection and real covariance matrix). For each part of this methodology, we varied the threshold to vary the number of variables that were kept and calculated for each threshold the True Positive Rate (TPR) and the False Positive Rate (FPR). The TPR is the number of variables that have been properly identified as being relevant for explaining the response divided by the total number of explanatory variables.

We also wanted to assess the sparsity: the percentage of non-zeros in the matrix B. Namely the percentage of pairs of input-output that actually interact together. To do this, we made different scenarios with high and low sparsity (0.01 and 0.3). For all of these scenarios we simulated 1000 different Y, so we performed all this methodology 1000 times each and we calculated at each time, for each methodology and for each threshold the TPR and the FPR. We then took the mean of this TPR and FPR for each methodology and for each threshold. We also assessed the importance of the stability selection.

We can see that our MultivarSel Strategy (Lasso empirical covariance) provides better results than sPLS and Lasso without covariance. Moreover, we observed that its performance is similar to Lasso with the real covariance matrix (the positive control), which means that we greatly estimated the dependence among the outputs. We also noted that the larger the sparsity level, the smaller the differences of performance between MultivarSel (Lasso empirical covariance) and Lasso without covariance, while the differences between Lasso empirical covariance and sPLS are bigger. We can see that adding the stability selection step improves a lot the results.

Modeling strategy

In order to select the most relevant inputs for modeling the outputs, we used the linear model methodology recently developed in Perrot-Dockès et al. (2018b) which has already been successfully applied to metabolomics data in Perrot-Dockès et al. (2018a). The great advantage of such an approach is to propose a Lasso-based criterion (Tibshirani, 1996) taking into account the dependence that may exist between the outputs. The parameters involved in the criterion are chosen thanks to 10-fold cross-validation and stability selection with 1000 resampling (Meinshausen and Bühlmann, 2010). The numerical experiments were performed using the real inputs dataset. Then, in order to mimic the Th groups, a random error matrix having a blockwise constant covariance matrix was generated.

The ROC curves display the True positive rate (TPR) as a function of the False positive rate (FPR) where the TPR is the number of variables that have been properly identified as being relevant for explaining the response divided by the total number of explanatory variables. The FPR is the number of variables that have been wrongly identified as being relevant for explaining the response divided by the total number of variables that do not explain the response. To look for a context dependent role of IL-12p70 in the presence of another input we performed the same methodology but instead of modeling the outputs by using only the inputs, some new variables were added: they correspond to a combination of IL-12p70 with the other inputs. More precisely, for instance, the variable "IL-12p70 with IL-1" is equal to the value of IL-12p70 for the samples having a positive concentration in IL-1 and to zero for the samples for which the concentration in IL-1 is equal to zero.

We propose the following modeling for the outputs:

$$Y = XB + E, \tag{1}$$

where $\boldsymbol{Y}$ denotes the $\boldsymbol{n}\times\boldsymbol{q}$ output matrix, $\boldsymbol{X}$ denotes the $\boldsymbol{n}\times\boldsymbol{p}$ design matrix containing the inputs, $\boldsymbol{B}$ is an unknown $\boldsymbol{p}\times\boldsymbol{q}$ coefficient matrix and $\boldsymbol{E}$ is the $\boldsymbol{n}\times\boldsymbol{q}$ random error matrix. Here, $\boldsymbol{n}$ corresponds to the number of samples, $\boldsymbol{q}$ is the number of outputs and $\boldsymbol{p}$ denotes the number of inputs. In order to take into account the potential dependence that may exist between the outputs, we shall assume that each row $\boldsymbol{i}$ of $\boldsymbol{E}$ satisfies:

$$(\boldsymbol{E}_{i,1},\ \ldots,\boldsymbol{E}_{i,q}) \sim \boldsymbol{N}(0, \boldsymbol{\Sigma_q}), \tag{2}$$

where $\boldsymbol{\Sigma_q}$ denotes the covariance matrix of the $\boldsymbol{i}$th row of the random error matrix.

In order to select the most relevant inputs for explaining the outputs, the methodology that we propose can be summarized in the following three steps:

First step

Fitting a multiple regression model to each output to have an estimation of the error matrix: $\widehat{\boldsymbol{E}}$ and computing its empirical covariance matrix.

Second step

Using this empirical covariance matrix to remove the dependence in $\boldsymbol{E}$, namely between the outputs.

Third step

Selecting among the inputs the most relevant for explaining the outputs by applying a Lasso approach to the transformed data as explained in the second step.

First step

Residuals and covariance matrix. We obtained an ordinary least square (OLS) estimator of $\boldsymbol{B}$ by fitting a multiple regression model which is not a variable selection method. More precisely, the corresponding estimator $\widehat{\boldsymbol{B}}^{\boldsymbol{OLS}}$ is defined by

$$\widehat{B}^{OLS} = Arg\min_{\mathbf{B}}\left\{\|Y - XB\|_2^2\right\}$$

Using $\widehat{\boldsymbol{B}}^{\boldsymbol{OLS}}$ we got an estimation of $\boldsymbol{E}$: $\widehat{\boldsymbol{E}} = \boldsymbol{Y} - \boldsymbol{X}\widehat{\boldsymbol{B}}^{\boldsymbol{OLS}}$. Then, we computed the empirical covariance matrix $\widehat{\boldsymbol{\Sigma}}_{\boldsymbol{q}}$ of $\widehat{\boldsymbol{E}}$.

Second step

Transformation. Let us recall that the standard Lasso criterion, proposed by Tibshirani (1996) estimates $\boldsymbol{B}$ in the following univariate linear model:

$$\boldsymbol{Y} = \boldsymbol{XB} + \boldsymbol{E}, \tag{3}$$

by

$$\widehat{B}(\lambda) = Argmin_B\left\{\|Y - XB\|_2^2 + \lambda\|B\|_1\right\}, \tag{4}$$

where $\boldsymbol{Y}$, $\boldsymbol{B}$ and $\boldsymbol{E}$ are vectors. Usually, the components of $\boldsymbol{E}$ are assumed to be independent.

Thus, we proposed to transform Model (1) to be able to use the Lasso criterion as follows. First, we removed the dependence among the outputs:

$$Y\widehat{\Sigma}_q^{-1/2} = XB\widehat{\Sigma}_q^{-1/2} + E\widehat{\Sigma}_q^{-1/2}, \tag{5}$$

where $\widehat{\boldsymbol{\Sigma}}_{\boldsymbol{q}}^{-1/2}$ denotes the inverse of the square root of $\boldsymbol{\Sigma_q}$.

Then, we applied the ***vec*** operator which consists in stacking the columns of a matrix into a single column vector.

$$\begin{aligned} Y &= vec\left(Y\widehat{\Sigma}_q^{-1/2}\right) = vec\left(XB\widehat{\Sigma}_q^{-1/2}\right) + vec\left(E\widehat{\Sigma}_q^{-1/2}\right) \\ &= vec\left(\left(\widehat{\Sigma}_q^{-1/2}\right)' \otimes X\right)vec(B) + vec\left(E\widehat{\Sigma}_q^{-1/2}\right) \\ &= Xb + \varepsilon. \end{aligned}$$

Third step: Variable selection

Thanks to the previous transformation, the Lasso criterion can be applied to $\boldsymbol{y} = \boldsymbol{vec}(\boldsymbol{Y}\widehat{\Sigma}_{\boldsymbol{q}}^{-1/2})$. Since $\boldsymbol{B} = \mathbf{vec}(\mathbf{B})$, estimating the coefficient of $\boldsymbol{B}$ boils down to estimating the coefficients of $\boldsymbol{B}$. The parameter λ in (4) is chosen by 10-fold cross-validation followed by a stability selection step with 1000 resamplings, as proposed by Meinshausen and Bühlmann (2010).

The squared error of prediction of the different models were assessed using 10-fold cross-validation (Figures 4A, 6B, S3D, S3E, and S5A).

Systematic literature review

To assess the literature and evaluate the generated multivariate model of Figure 4B, we conducted a systematic literature review to identify articles indexed on the PubMed database by March 1st 2017, examining the effects of inputs on naive CD4+ cells.

One of three different search strategies was used to export references from the PubMed database into the reference management software EndNote.

We started by performing the first search strategy which consisted of using free text to search English language articles for the input (or any of its aliases) and the output (or any of its aliases). If the search yielded 20 or less results, the references were exported into EndNote.

If not, then we performed the second search strategy, which consisted of searching English language articles for the input (or any of its aliases) and the output (or any of its aliases), both in the title or abstract, and at least one of the following medical subject heading terms: ''cell differentiation'' or ''CD4-positive T-lymphocytes'' or ''lymphocyte activation». If the search returned 50 or less results, the references were exported into EndNote. If not, then we carried out the third search strategy which returned English language articles that had both the input (or any of its aliases) and the output (or any of its aliases) in the title or abstract, as well as indexes to both of the following medical subject heading terms: ''cell differentiation'' and ''CD4-positive T-lymphocytes.'' Results were exported into EndNote.

The electronic searches generated a total of 14,748 references that were managed through EndNote. A manual search of references from review articles and other records identified 21 additional publications that were not included in the search results. Of these 14,769 articles, 9,780 duplicates were removed, leaving 4,989 records to be screened.

Titles and abstracts were screened by 2 independent reviewers. Publications were selected for further in-depth consideration if they met all of the following inclusion criteria: 1) Journal Article, 2) Examining the effect of one input at a time, 3) Testing on naive $CD4^+$ T cells, which were defined as $CD4^+$ and $CD45RA^+$ and/or $CD45RO^-$ and/or $CD25^-$ cells. Studies were excluded from the analysis if: 1) Full-text article, Title and/or abstract were not available, 2) Methods and/or experiments and/or results were unclear or inconclusive or of low quality. Reasons for removing articles included not performing proper experimental controls, insufficient information, lack of replicates and/or statistical analysis.

The reviewers excluded 4,589 articles because they did not meet the inclusion and exclusion criteria, leaving 400 articles of which, at least, the figures and materials and methods sections were examined. Finally, 178 publications met all the inclusion criteria and underwent data extraction.

Extracted information included the PubMed identifier, the input, the output, the input's effect on naive $CD4^+$ T cells in regards to the output, the experimental context and setup (e.g., details about T cell stimulation context, input's concentration, duration…) and the organism. Data were cross-checked by the 2 reviewers, and any ambiguities were discussed and resolved through a consensus.

The Exp Fold was not included in the literature review so it was not included in the following literature validation score.

Calculation of the literature validation score: an association predicted by our model (Figure 4B) between an input and an output was considered as ''new'' if none of the 178 publications found that the input induces or inhibits the output. Absence of effect depicted in some articles was not considered relevant to assess novelty of the prediction. It was ''validated'' if at least one of the 178 publications found similar results than our model and ''contradictory'' if none of the study found the same results than our model but at least one found an opposite result. Opposite result would be an induction if the model predicted a negative coefficient or an inhibition if our model predicted a positive coefficient.

DATA AND CODE AVAILABILITY

The dataset generated during this study is available in Table S2.

All references from literature mining are listed in Table S3.

Software used for flow cytometry data analysis was FlowJo software (TreeStar).

Software used for CBA analysis was FCAP Array v3.

Software used for statistical analysis was Prism software v5 (GraphPad).

Software used for statistical analysis and modeling was R version 3.5.2.

The R packages used to perform this study are: package MultiVarSel 1.0. used for modeling (available at https://cran.r-project.org/web/packages/MultiVarSel/index.html) and package TBoCo 0.0.1 for boxcox transformation available at https://github.com/Marie-PerrotDockes/TBoCo.

This study did not generate code.

A

Example of MoDC activation profile after 24 hours stimulation with Medium, LPS, Zymosan or Flu.
29 surface markers measured by flow cytometry shown on one representative donor.

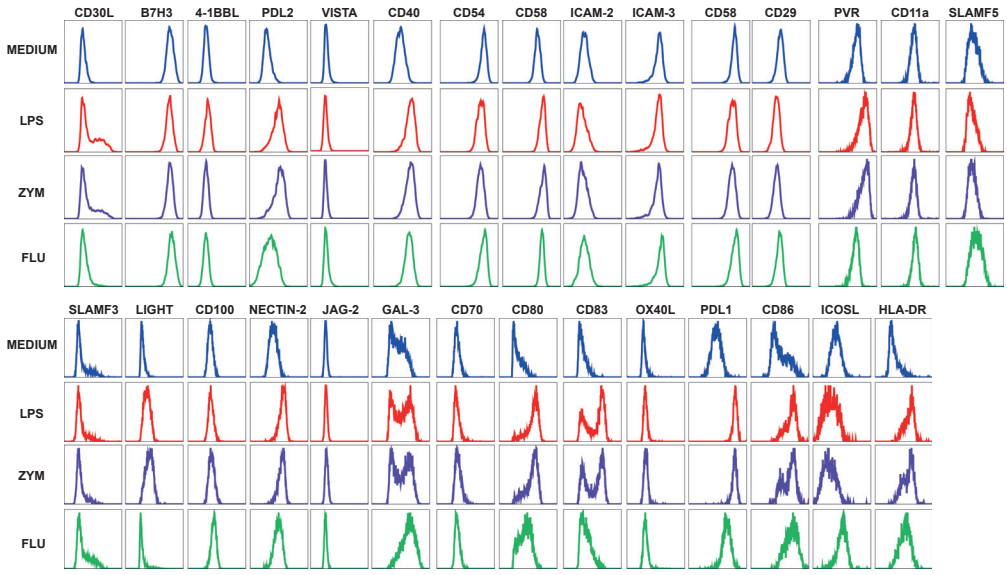

B

Comparison with Zymosan (10µg/mL)

	IL-23	IL-10	CD54	PVR
Medium	0.000	0.000	0.000	0.000
LPS (100ng/mL)	0.000	0.000	0.044	0.003
Flu (1X)	0.000	0.000	0.000	0.000

Comparison with LPS (100ng/mL)

	IL-12p70	CD83	CD30L
Medium	<0.001	<0.001	0.005
Zymosan (10µg/mL)	0.432	0.002	0.008
Flu (1X)	<0.001	0.002	0.002

Comparison with Flu (1X)

	IL-28α	ICOSL	CD18	CD100
Medium	<0.001	<0.001	<0.001	<0.001
LPS (100ng/mL)	<0.001	0.005	<0.001	0.017
Zymosan (10µg/mL)	<0.001	0.003	<0.001	0.017

Comparison with Medium

	CD86	CD80	HLA-DR
Zymosan (10µg/mL)	<0.001	<0.001	<0.001
LPS (100ng/mL)	<0.001	<0.001	<0.001
Flu (1X)	<0.001	<0.001	<0.001

C

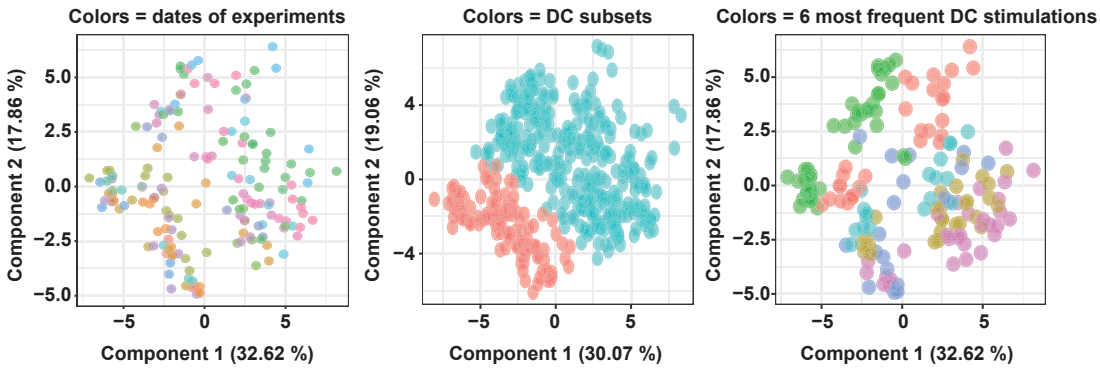

Figure S1. Descriptive Analysis of 36 DC-Derived Communication Molecules, Related to Figures 1 and 2

A) Example of raw FACS staining of MoDC communication molecules after 24 hours stimulation with Medium, LPS, Zymosan or Flu. 29 surface markers measured of one representative donor are shown. B) Statistical analysis comparing a given DC stimulation to the other 3 for each signal annotated. P values are annotated in the table, red should be considered as significant. Paired Wilcoxon test was used (n = 14). C) PCA performed either on the whole dataset (left and middle panel) or on the 6 most frequent perturbators (right panel) used across MoDC and bDC stimulations. From left to right colors respectively indicates, the dates of experiments, the DC subset, the 6 most frequent DC stimulations.

A

Input	Range (log)	% of positive observations	Coefficient of variation
IL-21	4.00	86.45	1.89
IL-10	4.00	97.43	1.78
IL-17F	4.00	75.23	1.75
IL-9	4.00	94.39	1.67
IL-5	4.00	99.53	1.07
IL-4	4.00	98.83	1.06
IL-13	4.00	97.66	0.92
IL-17A	3.00	83.18	1.77
IL-6	3.00	98.83	1.28
IFN-γ	3.00	97.20	1.08
IL-3	3.00	99.77	1.05
TNF-α	3.00	99.77	0.86
GM-CSF	3.00	100.00	0.72
IL-31	2.00	21.03	1.54
TNF-β	2.00	98.83	1.08
IL-22	2.00	57.94	0.98
IL-2	2.00	99.77	0.68
Expansion-fold	1.00	100.00	0.61

B

Comparison with Medium

	IL-2
Zymosan (10µg/mL)	0,7439
LPS (100ng/mL)	0,0535
Flu (1X)	0,0579

Comparison with Zymosan (10µg/mL)

	Expansion fold	IL-17A	IL-17F	IL-21
Medium	<0,001	<0,001	<0,001	0,0054
LPS (100ng/mL)	0,3007	0,0013	0,0127	0,1983
Flu (1X)	0,0093	<0,001	<0,001	1

Comparison with LPS (100ng/mL)

	IL-3	IL-9	IL-6	IFN-γ
Medium	0,0003	<0,001	0,2698	0,0858
Zymosan (10µg/mL)	0,082	0,5334	0,9814	0,1154
Flu (1X)	0,281	0,0072	0,1136	0,1279

	TNF-α	IL-22	IL-13	GM-CSF	TNF-β
Medium	0,3724	0,0579	0,0417	0,0008	0,1565
Zymosan (10µg/mL)	0,1823	0,2772	0,0019	<0,001	0,8342
Flu (1X)	0,1606	0,0188	0,4856	0,8391	0,0015

Comparison with Flu (1X)

	IL-4	IL-5	IL-10	IL-31
Medium	0,0584	0,0403	0,1287	0,0056
LPS (100ng/mL)	0,9769	0,504	0,1755	0,9149
Zymosan (10µg/mL)	0,0053	0,0003	0,2841	0,3998

C

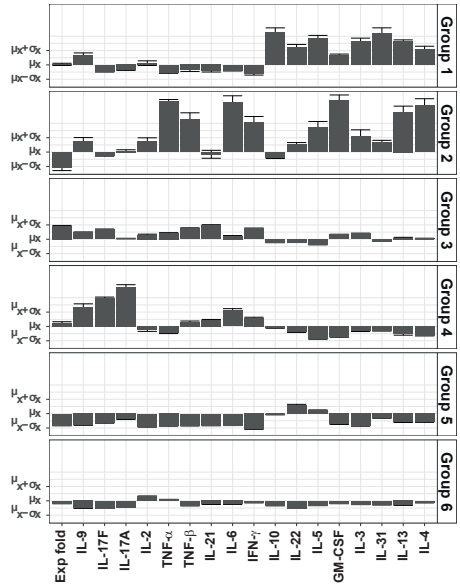

Figure S2. Mathematical Description and Statistical Analysis of Th Cytokine Profiles, Related to Figure 3

A) Table showing three key mathematical parameters of the Exp Fold and the 17 Th derived cytokines. First column: the range of expression (the number of log on which the data are expressed). Second column: the percentage of positive observations among the 428 datapoints. Third column: the coefficient of variation. Communication molecules were ranked based on their range of expression and their coefficient of variation. B) Statistical analysis comparing selected Th cytokines within the following groups: Medium-MoDC, LPS-MoDC, Zymosan-MoDC and Flu-MoDC. The statistical test used is paired Wilcoxon test on n = 14 donors. C) Expression profiles of the Exp Fold and the 17 Th derived cytokines within the six groups of DC conditions defined by hierarchical clustering. Expression data were logged transformed and scaled so as μ represents the mean and σ the SD of the expression of a given communication molecule across the whole dataset (n = 428).

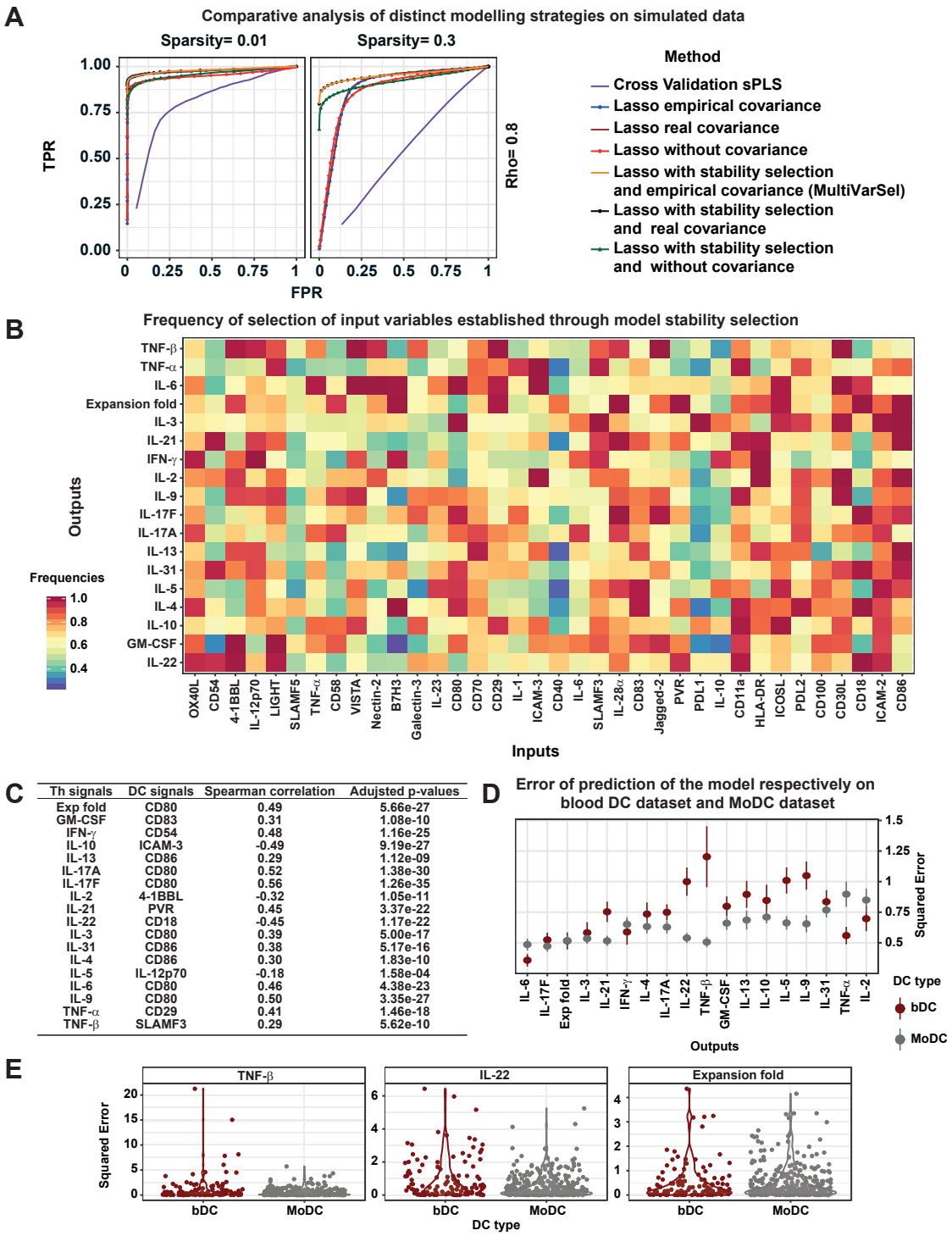

Th signals	DC signals	Spearman correlation	Adjusted p-values
Exp fold	CD80	0.49	5.66e-27
GM-CSF	CD83	0.31	1.08e-10
IFN-γ	CD54	0.48	1.16e-25
IL-10	ICAM-3	-0.49	9.19e-27
IL-13	CD86	0.29	1.12e-09
IL-17A	CD80	0.52	1.38e-30
IL-17F	CD80	0.56	1.26e-35
IL-2	4-1BBL	-0.32	1.05e-11
IL-21	PVR	0.45	3.37e-22
IL-22	CD18	-0.45	1.17e-22
IL-3	CD80	0.39	5.00e-17
IL-31	CD86	0.38	5.17e-16
IL-4	CD86	0.30	1.83e-10
IL-5	IL-12p70	-0.18	1.58e-04
IL-6	CD80	0.46	4.38e-23
IL-9	CD80	0.50	3.35e-27
TNF-α	CD29	0.41	1.46e-18
TNF-β	SLAMF3	0.29	5.62e-10

Figure S3. Multivariate Modeling Strategies Applied to Our DC-T Cell Datasets, Related to Figure 4

A) Comparative analysis of distinct modeling strategies on simulated data. Using ROC curves, we applied the annotated strategies in terms of true and false discovery. The simulated dataset mimics the features of our DC and T cell experimental data but for which we artificially attributed a link between DC signals and Th cytokines. This allowed us to compare four different types of modeling strategies (Raw, OR, MultivarSel and sPLS) and different variable selection methods (Lasso, Stability Selection and CV) by analyzing their false and true positive rates. B) Frequency of selection of input variables established through model stability selection. Stability selection was applied after our MultivarSel strategy to the full DC-T dataset (n = 428). C) Table

(legend continued on next page)

showing for each output (Th signals) the input that minimizes its mean squared error of prediction in an univariate model, with its spearman correlation coefficient and its adjusted p value. D) Error of prediction (obtained by 10-fold cross-validation) of the model respectively on blood DC dataset (n = 118) and MoDC dataset (n = 310) E) Example of distribution of the squared error of prediction per DC-type for IL-22, TNF-β and Exp Fold. Allows to see the number of data points with the highest error of prediction.

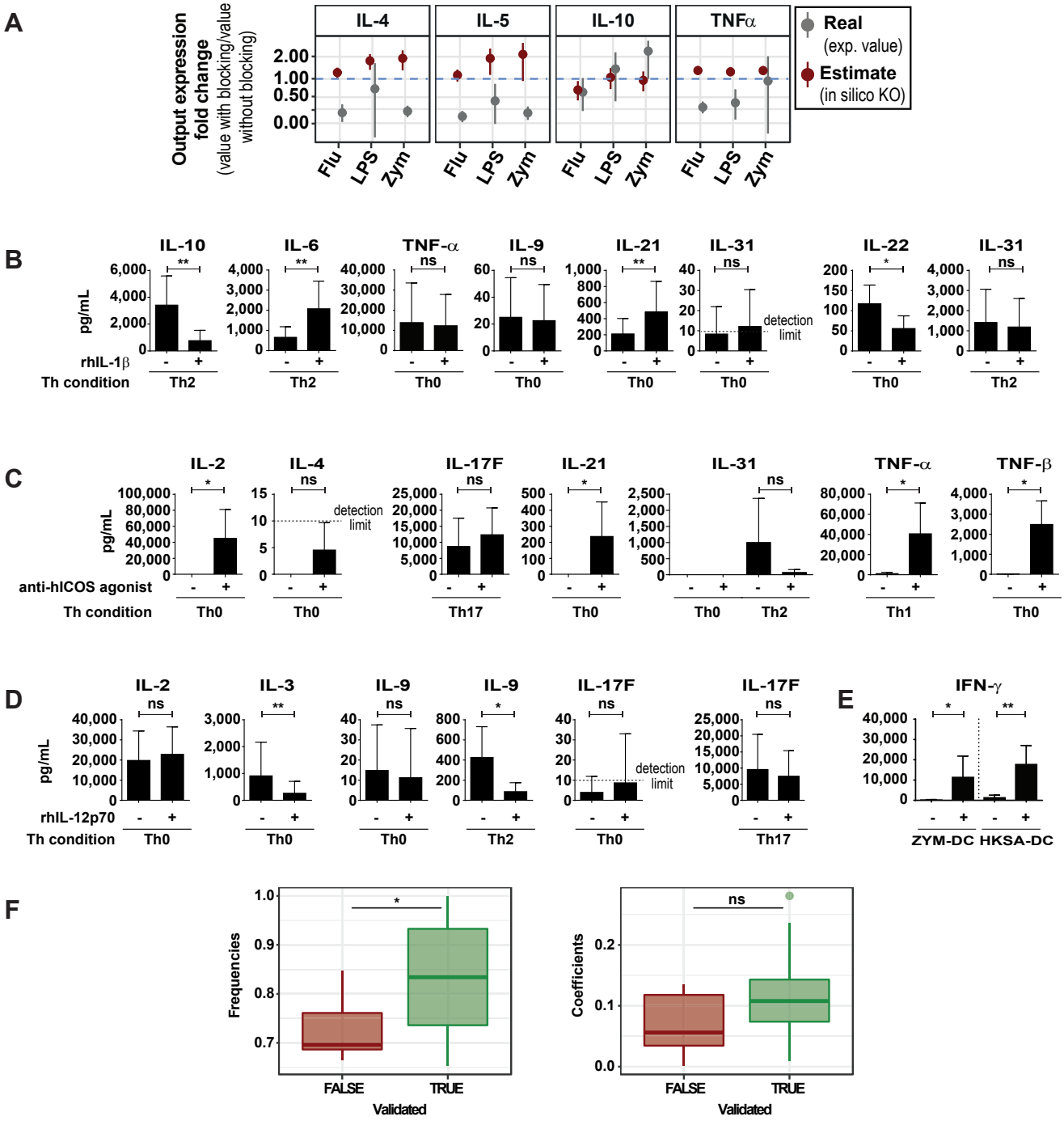

Figure S4. Complementary Th Secretion Profiles of the Tested Conditions for Systematic Model Validation, Related to Figure 5

A) Fold change of the cytokine concentration estimated versus experimentally measured for the four indicated cytokines. n = 6 independent donors B) Mean cytokine concentration and SD indicated for each condition. n = 6 C) Mean cytokine concentration and SD indicated for each condition. n = 6 D) and E) Mean cytokine concentration and SD indicated for each condition. n = 6 F) Boxplot of the coefficient and stability selection frequencies in the two conditions: True (validated predictions) and False (not validated), Wilcoxon test. Performed only for IL-12, IL-1 and ICOSL validations.

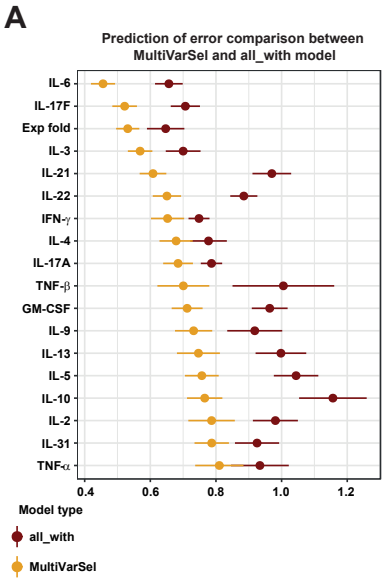

B

Intputs	Number	Number alone	Number with	Percentage
CD70	638	580	58	0.09
CD11a	673	611	62	0.09
ICOSL	609	551	58	0.10
OX40L	622	562	60	0.10
IL-28α	607	545	62	0.10
CD83	539	482	57	0.11
LIGHT	607	534	73	0.12
CD30L	606	533	73	0.12
ICAM-2	684	601	83	0.12
IL-23	389	339	50	0.13
Jagged-2	484	420	64	0.13
CD100	452	392	60	0.13
4-1BBL	482	418	64	0.13
VISTA	433	374	59	0.14
PDL2	493	420	73	0.15
IL-12p70	582	494	88	0.15
PVR	360	304	56	0.16
SLAMF3	515	433	82	0.16
TNF-α	416	346	70	0.17
CD86	569	471	98	0.17
CD80	440	362	78	0.18
HLA-DR	505	411	94	0.19
Nectin-2	316	254	62	0.20
IL-1	384	301	83	0.22
CD58	383	289	94	0.25
CD18	415	311	104	0.25
CD29	453	335	118	0.26
CD54	238	175	63	0.26
CD40	251	182	69	0.27
ICAM-3	454	325	129	0.28
IL-6	295	210	85	0.29
B7H3	432	307	125	0.29
Galectin-3	333	220	113	0.34
IL-10	241	159	82	0.34
PDL1	207	121	86	0.42
SLAFM5	217	72	145	0.67

C

Outputs	Number	Number alone	Number with	Percentage
IL-2	926	806	120	0.13
IL-4	932	802	130	0.14
IL-6	1013	865	148	0.15
IL-3	912	777	135	0.15
IL-13	741	631	110	0.15
GM-CSF	920	780	140	0.15
TNF-β	838	710	128	0.15
IL-10	1103	901	202	0.18
TNF-α	607	495	112	0.18
IL-17A	947	772	175	0.18
IL-17F	1030	839	191	0.19
IL-31	1088	884	204	0.19
IL-21	848	677	171	0.20
IL-9	955	762	193	0.20
Exp fold	1041	828	213	0.20
IL-5	773	613	160	0.21
IL-22	968	767	201	0.21
IFN-γ	682	535	147	0.22

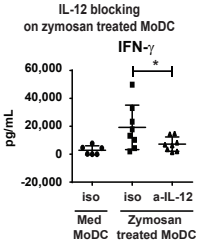

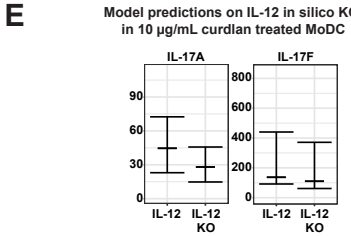

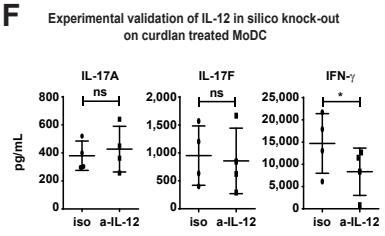

Figure S5. Quantification of Context-Dependent Input-Output Associations, Related to Figure 6

A) Prediction of error comparison between MultiVarSel and "all_with model" performed for each Th output. B) Quantification per input of the number of times it is selected as associated to an output in the 36 context-dependent models (Table S5). The total number of associations (resp. the number associations of the input alone, resp. the input with another) is represented in the column 'Number' (resp. Number alone, resp. Number with) the ratio (Number with / Number) is represented in the column 'Percentage' C) Same as panel B but per output instead of input. D) On 8 distinct donors of coculture MoDC/naive CD4 T cells experiments IL-12 was blocked using neutralizing antibody. After the coculture at day 6, Th cells were restimulated 24 hours at 1 million cells/mL and the amount of IFN-γ was determined using CBA. Paired Student's t test was applied to compare two conditions. E) Model predictions on IL-12 *in silico* KO in the condition MoDC-curdlan (10 µg/mL) for IL-17A and IL-17F values. Real values in the presence of IL-12 are compared to predicted values obtained in the absence of IL-12. F) Concentrations of IL-17A, IL-17F and IFN-γ produced by Th cells after coculture with MoDC treated with 10 µg/mL curdlan, in the presence of neutralizing antibody specific for IL-12 or matching isotype. n = 4 donors. Paired t test was performed to compare the means.

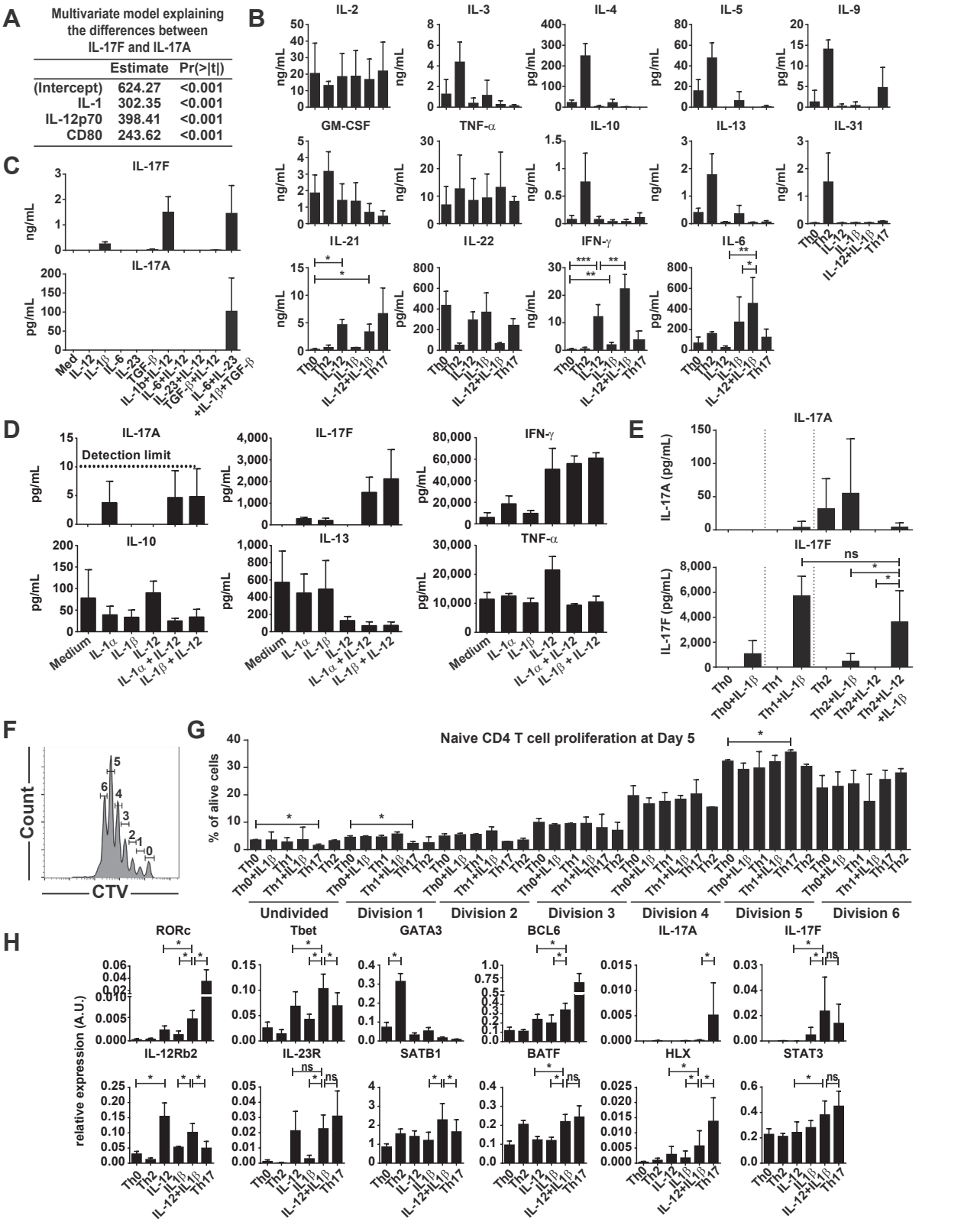

(legend on next page)

Figure S6. In-Depth Characterization of Th Cells Polarized under the IL-1+IL-12 Condition, Related to Figure 7

A) Multivariate model explaining the differences between IL-17F and IL-17A for a stability selection threshold of 0.8. B) Cytokine profiles of Th cells differentiated in distinct cytokine condition: Th0 (medium), Th2 (IL-4), IL-12, IL-1 (IL-1β), IL-12+IL-1 and Th17 (IL-6+IL-1β+TGF-β+IL-23), measured by CBA on 6 donors. Paired Student's t test was used for statistical analysis. C) IL-17A and IL-17F were measured by CBA in the supernatants of Th cells differentiated in distinct cytokine condition: Med, IL-12, IL-1β, IL-6, IL-23, TGF-β, IL-12+IL-1β, IL-6+IL-12, IL-23+IL-12, TGF-β+IL-12, IL-6+IL-23+IL-1β+TGF-β. This experiment was performed on 3 donors. D) Comparison in the same naive CD4 DC-free culture system of the effect of IL-1α and IL-1β on the production of six distinct cytokines: IFN-γ, IL-17A, IL-17F, TNF-α, IL-13, IL-10. This experiment was performed on 3 donors. E) DC-free differentiation assay performed using anti CD3/CD28 beads in the indicated cytokine conditions. n = 6, Wilcoxon test was used for statistics. F) Example of FACS CTV staining for Th proliferation assessment at day 5. G) Quantification of the % of alive cells in each peak of the CTV staining for each condition. n = 3, paired t test was performed H) qPCR expression profiles for selected genes in the following conditions Th0, Th2, IL-12, IL-1β, IL-12+IL-1β, Th17 (IL-6+IL-23+IL-1β+TGF-β). n = 6. Wilcoxon test was used.

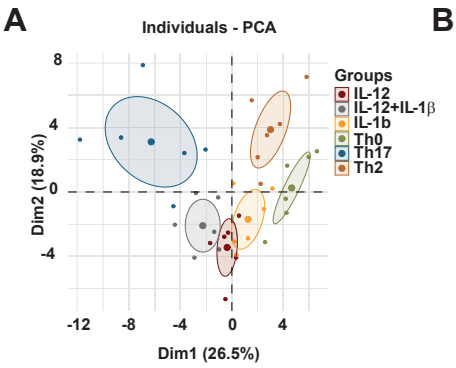

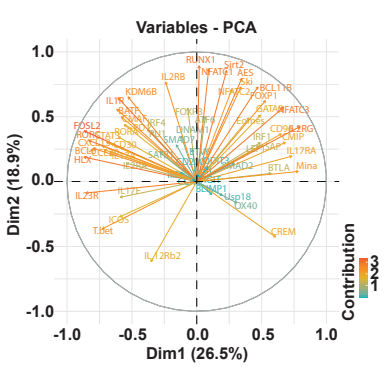

C

Inputs	Number	Correlation of IL-12 with IL-17A	p-value
IL-1	166	0.41	3.51e-08
CD70	120	0.41	3.09e-06
OX40L	181	0.39	6.44e-08
IL-6	226	0.37	1.22e-08
IL-10	207	0.36	9.06e-08
IL-23	234	0.36	1.51e-08
ICAM-2	149	0.36	7.86e-06
LIGHT	119	0.33	2.02e-04
Jagged-2	194	0.33	2.11e-06
TNF-α	205	0.31	6.30e-06
CD30L	183	0.28	9.24e-05
IL-28α	22	-0.24	2.84e-01

D

Group	Correlation of IL-12 with IL-17A	p-value
IL-23 & IL-1	0.41	3.51e-08
IL-23 & no IL-1	-0.01	9.52e-01
no IL-23 & IL-1	-0.37	2.90e-01
no IL-23 & no IL-1	-0.16	3.02e-02

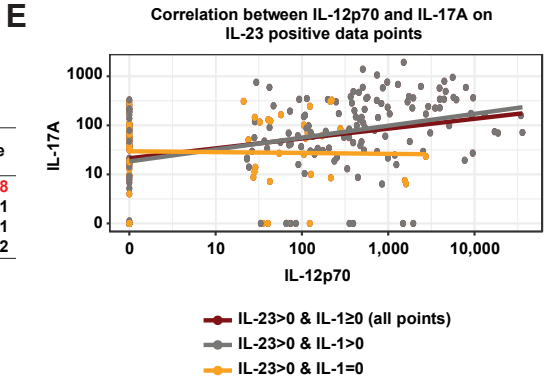

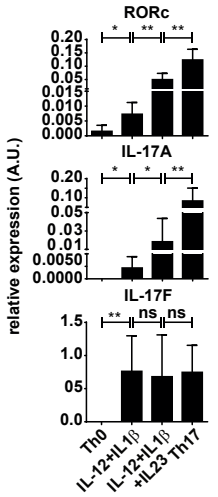

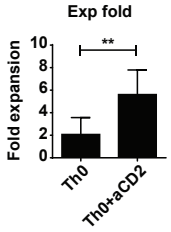

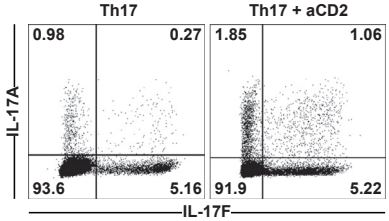

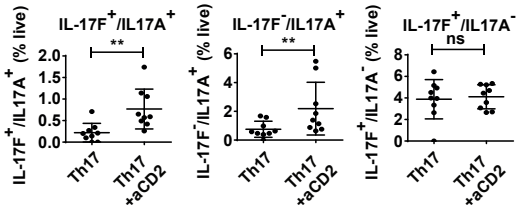

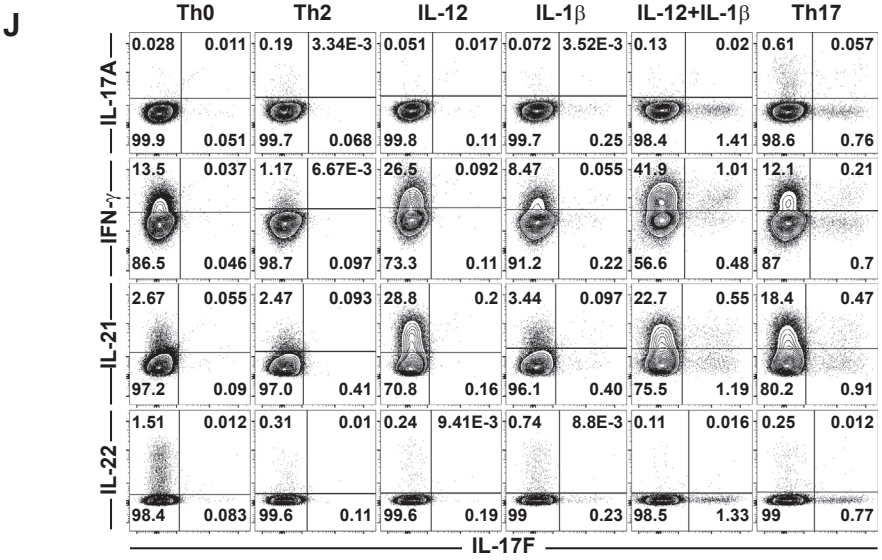

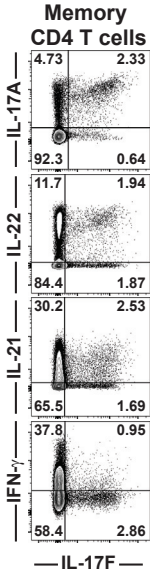

(legend on next page)

Figure S7. Detailed Description of Distinct Experimentally Validated Predictions,

A) PCA using 63 genes measured by qPCR in the 6 indicated Th conditions B) Detailed descriptions of the contribution of each 63 genes to the two first dimensions of the PCA represented in A). C) Systematic univariate analysis evaluating the Pearson correlation between IL-17A and IL-12 in the presence of IL-23 and another input (listed in the column 'Inputs') the number of samples having both of these inputs is in column 'Number'. D) Pearson correlation between IL-17A and IL-12 in the presence or absence of IL-1 and IL-23. E) Dot plot representing the correlation between IL-12 and IL-17A on IL-23 positive data points. F) qPCR measuring RORc, IL-17A and IL-17F in the indicated conditions. n = 6 independent donors. Wilcoxon test was used for statistical analysis G) Positive control showing the validation of the anti-CD2 agonist antibody through the measure of Exp Fold in the Th0 condition n = 8 H) Representative intracellular cytokine staining for IL-17A and IL-17F performed in the Th17 and Th17+anti-CD2 conditions. I) Quantification of the intracellular FACS staining performed in H) for 8 distinct donors. Wilcoxon analysis. J) Representative raw data staining of intracellular FACS for IFN-γ, IL-21, IL-22, IL-17A and IL-17F in 6 distinct conditions, Th0 (medium), Th2 (IL-4), IL-12, IL-1 (IL-1β), IL-12+IL-1 and Th17 (IL-6+IL-1β+TGF-β+IL-23) for naive CD4 culture. K) Representative raw data staining of intracellular FACS for IFN-γ, IL-21, IL-22, IL-17A and IL-17F for memory CD4 purified cells, previously isolated by magnetic sorting, and restimulated 5 hours with PMA/ionomycin.